

**REPUBLIC OF TURKEY
YILDIZ TECHNICAL UNIVERSITY
GRADUATE SCHOOL OF NATURAL AND APPLIED SCIENCES**

SCATTERING FROM PARTIALLY BURIED OBJECTS



UĞUR SAYNAK

**PhD. THESIS
DEPARTMENT OF ELECTRONIC AND COMMUNICATIONS
ENGINEERING
PROGRAM OF COMMUNICATIONS**

**ADVISER
PROF. DR.AHMET KIZILAY**

İSTANBUL, 2016

REPUBLIC OF TURKEY
YILDIZ TECHNICAL UNIVERSITY
GRADUATE SCHOOL OF NATURAL AND APPLIED SCIENCES

SCATTERING FROM PARTIALLY BURIED OBJECTS

A thesis submitted by Uğur SAYNAK in partial fulfillment of the requirements for the degree of **DOCTOR OF PHILOSOPHY** is approved by the committee on 11.08.2016 in Department of Electronic and Communications Engineering, Communications Program.

Thesis Adviser

Prof. Dr. Ahmet KIZILAY
Yıldız Technical University

Approved By the Examining Committee

Prof. Dr. Ahmet KIZILAY
Yıldız Technical University

Prof. Dr. Filiz GÜNEŞ
Yıldız Technical University

Assoc. Prof. Dr. İsmail H. Tayyar
Karabük University

Assoc. Prof. Dr. Salih Demirel
Yıldız Technical University

Assoc. Prof. Dr. Senem Makal Yücedağ
TÜBİTAK

ACKNOWLEDGEMENTS

I would like to thank to my advisor, Prof.Dr. Ahmet KIZILAY, for his support and advices. He has guided me through the dissertation process with good ideas and supporting positive motivation.

I'd also like to thank to especially to my family for their continuous encouragement and support.

August, 2016

Uğur SAYNAK

TABLE OF CONTENTS

	Page
LIST OF SYMBOLS	vi
LIST OF ABBREVIATIONS.....	vii
LIST OF FIGURES	viii
CHAPTER 1	
INTRODUCTION	1
1.1 Literature	1
1.2 Objective of the Thesis.....	1
1.3 Hypothesis.....	2
CHAPTER 2	
SCATTERING FROM A CYLINDRICAL DISCONTINUITY ON A PERFECTLY CONDUCTING INFINITE GROUND PLANE	3
2.1 Introduction.....	3
2.2 Analytical Solution for Scattering from a Circular Bump	4
2.3 Method of Moments Solution for Scattering from an Arbitrary Bump	5
2.4 Solution by the Decomposition Method	8
2.5 Numerical Results	11
CHAPTER 3	
SCATTERING FROM AN OVERFILLED CYLINDRICAL CAVITY ON A PERFECTLY CONDUCTING INFINITE GROUND PLANE.....	17
3.1 Introduction	17
3.2 Literature	18
3.3 Solution by the Decomposition Method	18
3.4 Numerical Results	20
CHAPTER 4	

SCATTERING FROM A PERFECTLY CONDUCTING CYLINDER PARTIALLY BURIED IN A DIELECTRIC HALF SPACE	26
4.1 Introduction	26
4.2 Solution by the Decomposition Method	27
4.3 Numerical Results	30
CHAPTER 5	
SCATTERING FROM A CYLINDER PARTIALLY BURIED IN A DIELECTRIC HALF SPACE WITH AN ARBITRARY PERIODIC BOUNDARY PLANE PROFILE	35
5.1 Introduction.....	35
5.2 Scattering from a Dielectric Half Space with a Periodic Boundary Surface	36
5.3 Solution by the Decomposition Method	39
5.4 Numerical Results	42
CHAPTER 6	
CONCLUSIONS	50
REFERENCES	51
APPENDIX-A	54
CALCULATION OF SELF TERMS	54
CURRICULUM VITAE.....	56

LIST OF SYMBOLS

\vec{A}	Magnetic vector potential
\vec{F}	Electrical vector potential
\vec{E}	Electric field vector
\vec{H}	Magnetic field vector
\vec{J}	Electrical current density
\vec{M}	Magnetic current density
ϵ	Dielectric permittivity
μ	Magnetic permeability
σ_e	Electrical conductivity
σ	Radar cross width or section
k	Wavenumber
λ	Wavelength
η	Characteristic impedance
φ	Polar angle
$\vec{\rho}$	Position vector
S	Surface
\hat{I}	Unit vector tangent to a surface
\hat{n}	Normal vector of a surface

LIST OF ABBREVIATIONS

E-field	Electric Field
EFIE	Electric Field Integral Equation
MoM	Method of Moments
PEC	Perfectly Electrical Conducting
TM	Transverse Magnetic

LIST OF FIGURES

		Page
Figure 2.1	Bump geometry	3
Figure 2.2	Indent geometry	4
Figure 2.3	Linear segmentation on the cylindrical bump surface.....	7
Figure 2.4	Demonstration of the vanished ground plane region.....	9
Figure 2.5	Monostatic scattering width of a semi-circular bump with a radius of λ	11
Figure 2.6	Convergence of the solution with strip length l	12
Figure 2.7	Current distribution comparison for $l / \lambda = 5$	13
Figure 2.8	Triangular bump geometry	14
Figure 2.9	Monostatic scattering width of a triangular bump.....	14
Figure 2.10	Calculation results for the semi-circular cavity.....	15
Figure 2.11	Semi-elliptical cavity geometry.....	15
Figure 2.12	Calculation results for the semi-elliptical cavity.....	15
Figure 2.13	The rectangular and triangular cavities	16
Figure 2.14	Calculation results for the rectangular and triangular cavities	16
Figure 3.1	Scattering geometry.....	18
Figure 3.2	Application of the equivalency principle on the scatterer, (a) upper equivalence, (b) internal equivalence.....	19
Figure 3.3	Scattering width of a semicircular bump with radius λ on an infinite perfectly conducting ground plane.....	21
Figure 3.4	Perturbated current density on S_1 for various incidence angles	21
Figure 3.5	Geometry for scattering by a triangular cavity in an infinite ground plane	22
Figure 3.6	Results for scattering by a triangular cavity in an infinite ground plane	22
Figure 3.7	Scattering geometry for monostatic scattering by a material loaded elliptical cavity in an infinite ground plane.....	23
Figure 3.8	Results for monostatic scattering by a material loaded cavity in an infinite ground plane	23
Figure 3.9	Scattering geometry for bistatic scattering by a material loaded elliptical cavity in an infinite ground plane.....	24
Figure 3.10	Results for bistatic scattering by a material loaded cavity in an infinite ground plane.....	24
Figure 3.11	Results for monostatic scattering by a lossy material loaded cavity on an infinite ground plane	25
Figure 4.1	Scattering geometry.....	26
Figure 4.2	Application of the equivalency principle on the scatterer, (a) upper equivalence, (b) lower equivalence.....	28
Figure 4.3	Demonstration of the vanished boundary plane region.....	28

Figure 4.4	Scattering width of a half-buried circular cylinder with radius λ	31
Figure 4.5	Current induced on a PEC circular cylinder half-buried in a material with $\epsilon_r = 4$, $\mu_r = 1$ and $\sigma_e = 0$ for different incidence angles.....	31
Figure 4.6	Current induced on a half-buried PEC rectangular cylinder for different medium parameters	32
Figure 4.7	Perturbated current densities for green curve on Figure 4.6	32
Figure 4.8	Range profiles for the half-buried square cylinder.....	33
Figure 4.9	Geometry for analyzing the range profile	34
Figure 5.1	Scattering geometry.....	35
Figure 5.2	Periodic boundary interface surface	36
Figure 5.3	Application of the equivalency principle on the scatterer, (a) upper equivalence, (b) lower equivalence and (c) internal equivalence	40
Figure 5.4	Current density distribution on the periodic surface for one period.....	43
Figure 5.5	Electrical current density distribution on the periodic surface for one period.....	44
Figure 5.6	Magnetic current density distribution on the periodic surface for one period.....	44
Figure 5.7	Scattering width of a semicircular bump with radius λ on an infinite perfectly conducting ground plane with periodic sinusoidal interface surface height profile.....	45
Figure 5.8	Geometry of a circular cylinder with material properties of free space, semi-buried in a half space with free space parameters.....	45
Figure 5.9	Scattering width of a circular cylinder with electrical properties of free space, semi-buried in a half space with electrical properties of free space	46
Figure 5.10	Normalized electrical current density induced on a highly electrically conducting circular cylinder half-buried in a material half space with electrical parameters $\epsilon_{r2} = 1$, $\mu_{r2} = 1$ and $\sigma_{e2} = 0$	47
Figure 5.11	Results for monostatic scattering by a semi-buried dielectric elliptical cylinder.....	47
Figure 5.12	Results for bistatic scattering by a semi-buried dielectric elliptical cylinder.....	48
Figure 5.13	Scattering geometry for monostatic scattering by a semi-buried dielectric circular cylinder	49
Figure 5.14	Scattering width of a circular cylinder with electrical properties $\epsilon_{r1} = 2$, $\mu_{r1} = 1$ and $\sigma_{e1} = 0$, semi-buried in a half space with electrical properties $\epsilon_{r2} = 4$, $\mu_{r2} = 1$ and $\sigma_{e2} = 0$	49
Figure A.1	Evaluation of Principle Value	55

SCATTERING FROM PARTIALLY BURIED OBJECTS

Uğur SAYNAK

Department of Electronics and Communications Engineering

PhD. Thesis

Adviser: Prof. Dr. Ahmet KIZILAY

Scattering from a dielectric object of arbitrary cross section partially buried in a dielectric half space having a periodic rough interface is investigated with a new numerical method which simplifies solution of the problem compared with other solution methods. Proposed method is to be used to solve two-dimensional problems for TM_z polarization.

In the proposed solution method, the absence and the presence of the scatterer is considered separately. In the presence of the scatterer, it is assumed that perturbed electrical and magnetic current densities exists on a finite perturbation region on the surface that separates the dielectric half space and free space, near the scatterer. The interaction of this perturbation region and the scatterer are considered, then current densities on the perturbation surface and the scatterer are calculated by the proposed method in frequency domain. The equivalency principle and a perturbation approach are used to get integral equations, and the Method of Moments is used to solve these integral equations.

Keywords: Electromagnetic fields, The Method of moments, equivalency principle, perturbation fields, integral equations.

**KISMİ GÖMÜLÜ CİSİMLERDEN SAÇILAN
ELEKTROMAGNETİK ALANLARIN HESAPLANMASI**

Uğur SAYNAK

Elektronik ve Haberleşme Mühendisliği Anabilim Dalı

Doktora Tezi

Tez Danışmanı: Prof. Dr. Ahmet KIZILAY

Engebeli ve dielektrik bir ortamın içinde kısmi gömülü keyfi bir kesite sahip bir dielektrik cisimden elektromanyetik saçılma iki boyutlu durum ve TM_z polarizasyon için pertürbasyon yaklaşımı ile çözülecektir. Bu yaklaşım problemin çözümünü diğer çözüm yöntemlerine kıyasla basitleştirmektedir.

Sunulan çözüm yöntemi problemi saçıcının olması ve olmaması durumunu gözönüne alarak, saçıcının bulunması durumunda dielektrik yarı uzayı boş uzaydan ayıran sınır yüzeyi üzerinde sonlu bir pertürbasyon bölgesinde fark akım yoğunluklarının ortaya çıktığını varsaymaktadır. Pertürbasyon yüzeyi ve saçıcı cismin etkileşimi gözönüne alınarak eşdeğerlik prensibi ve moment metodu yardımıyla cismin üzerindeki akımların ve rahatsızlık akımlarının hesaplanması frekans domaninde gerçekleştirildi. Eşdeğerlik prensibi ve pertürbasyon yaklaşımı integral denklemlerinin elde edilmesinde, Moment Metodu ise elektrik ve manyetik akım yoğunluklarının bu denklemler ile bulunmasında kullanılmıştır.

Anahtar Kelimeler: Elektromanyetik alanlar, Moment Metodu, eşdeğerlik prensibi, perturbasyon alanları, integral denklemleri.

INTRODUCTION

1.1 Literature

The topic of electromagnetic scattering from a partially-buried object in a lossy half space is studied by several researchers. Several techniques for solving this problem are introduced. Practical applications of this problem are mainly ground-penetrating radar applications, such as, detection and imaging of buried objects with some part over the ground.

There have been many works dealing with buried objects in the literature, as well as objects over a half space, which are similar in principle. Numerical simulation of scattering from a semi-buried object in a flat interface plane is available in the literature, [1]-[7]. The Method of Moments (MoM) solution for a perfectly conducting cylinder with arbitrary cross section [2] is a good example, which is numerically exact, but solution involves complex formulations and Sommerfeld integrals. Scattering from an object, which is in a multilayer/stratified media [8] is similar to afore mentioned works, with many examples in the literature. For the case when the interface has a roughness, there are several solutions available in the literature [9]-[10].

1.2 Objective of the Thesis

The objective of the thesis is to solve electromagnetic scattering from an object semi-buried in a lossy half space, which has a periodic boundary interface by using a perturbation technique [11], [12], [13] with the equivalence principle of the electromagnetic theory with a simple formulation. The solution procedure is called “The Decomposition Method” and applied to the TM_z scattering problems. This method is employed to acquire a set of Electrical Field Integral Equations (EFIEs), then the

Method of Moments is used to solve these equations with point matching and pulse basis functions.

1.3 Hypothesis

When applying the decomposition method to the problem of scattering from a semi-buried cylindrical object, it is assumed that the effect of the object on the interface, which is called perturbation on the boundary plane, is rapidly decaying with distance. Putting the scattering object into the interface also causes perturbational fields due to “vanished” current densities that exist when there is not an object present. The EFIEs are solved in the frequency domain using MoM.



SCATTERING FROM A CYLINDRICAL DISCONTINUITY ON
A PERFECTLY CONDUCTING INFINITE GROUND PLANE

2.1 Introduction

In this section problem of electromagnetic scattering from an arbitrary bump or an indent on a perfectly conducting infinite flat ground plane is examined with the decomposition method. Firstly, series solution for a bump with circular cross section is introduced, and then MoM solution of a bump with arbitrary cross section is presented. Afterwards application of the decomposition method is outlined. Lastly, several numerical examples are presented for validation.

Scattering problems are two-dimensional arbitrary discontinuities on an infinite perfectly conducting ground plane, as depicted on Figure 2.1 and Figure 2.2.

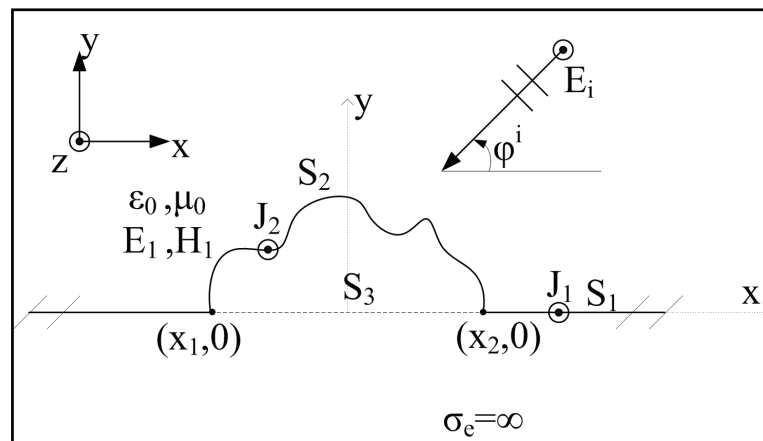


Figure 2.1 Bump geometry

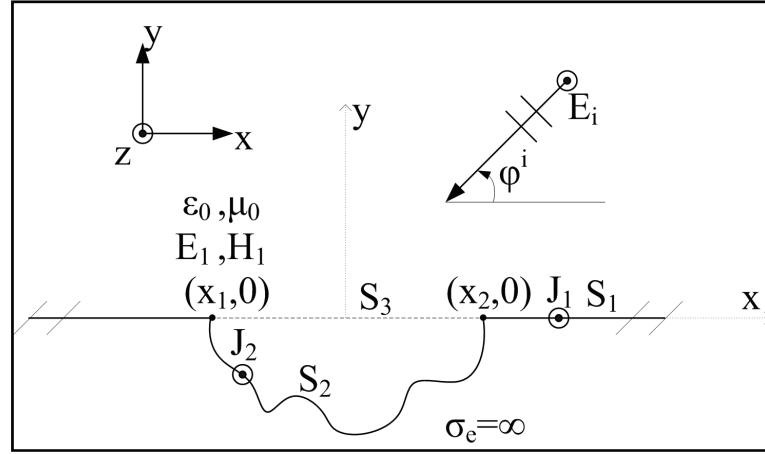


Figure 2.2 Indent geometry

Here S_2 is the bump or cavity cross-section surface, S_3 is the surface that will be absent when the discontinuity is present, and S_1 is the infinite perfectly conducting plane lying on the x axis. A TM_z polarized plane wave with E-field component

$$\vec{E}^i = e^{jk_0(x\cos\phi^i + y\sin\phi^i)} \hat{z} \quad (2.1)$$

is incident on discontinuity with arbitrary cross-section with the incidence angle ϕ^i . Here, k_0 is the free space wavenumber.

2.2 Analytical Solution for Scattering from a Circular Bump

Consider an incident unity amplitude TM_z polarized E-field component of a plane wave with the cylindrical wave representation [14]:

$$\vec{E}^i = e^{jk_0\rho\cos(\varphi-\phi^i)} \hat{z} = \sum_{n=-\infty}^{\infty} j^n J_n(k_0\rho) e^{jn(\varphi-\phi^i)} \hat{z}, \quad (2.2)$$

where $J_n(\cdot)$ is the Bessel function of order n , is incident on a semi-circular bump with radius a . Total E-field should be summation of incident, reflected and scattered field:

$$\vec{E}^{Total} = \vec{E}^i + \vec{E}^{ref} + \vec{E}^s \quad (2.3)$$

Where the reflected E-field:

$$\vec{E}^{ref} = -e^{jk_0\rho\cos(\varphi+\phi^i)} \hat{z} = -\sum_{n=-\infty}^{\infty} j^n J_n(k_0\rho) e^{jn(\varphi+\phi^i)} \hat{z}, \quad (2.4)$$

and the scattered E-field should be of the form:

$$\vec{E}^s = \sum_{n=-\infty}^{\infty} a_n H_n^{(2)}(k_0 \rho) e^{jn\varphi} \hat{z}, \quad (2.5)$$

where $H_n^{(2)}(\cdot)$ is the Hankel function of second kind of order n . Total field should satisfy:

$$\vec{E}^{Total} \Big|_{\rho=a} = \sum_{n=-\infty}^{\infty} \left\{ j^n J_n(k_0 a) \left[e^{jn(\varphi-\varphi^i)} - e^{jn(\varphi+\varphi^i)} \right] + a_n H_n^{(2)}(k_0 a) e^{jn\varphi} \right\} \hat{z} = 0, \quad (2.6)$$

this leads to:

$$a_n = -2 \frac{j^{1+n} J_n(k_0 a) \sin n\varphi^i}{H_n^{(2)}(k_0 a)}. \quad (2.7)$$

The scattered field is can be calculated using large argument form of the Hankel function and equation (2.5) in the far-field region ($\rho \rightarrow \infty$):

$$\vec{E}^s \cong \sqrt{\frac{2j}{\pi k_0 \rho}} e^{-jk_0 \rho} \sum_{n=-\infty}^{\infty} a_n e^{jn(\varphi-\pi/2)} \hat{z} \quad (2.8)$$

2.3 Method of Moments Solution for Scattering from an Arbitrary Bump

Scalar wave equation involving z directed component of the magnetic vector potential and a line source positioned at (x_0, y_0) :

$$(\Delta + k_0^2) A_z(x, y) = -\mu_0 J_0 \delta(x - x_0) \delta(y - y_0), \quad (2.9)$$

where Δ is the Laplacian operator and $\delta(\cdot)$ is the Dirac delta function. Fourier transform of equation (2.9) with respect to x with the spectral variable k_x leads to the ordinary differential equation:

$$\left(\frac{\partial^2}{\partial y^2} + k_0^2 - k_x^2 \right) \tilde{A}_z(k_x, y) = -\mu_0 J_0 \delta(y - y_0) e^{jk_x x_0}, \quad (2.10)$$

which has a solution:

$$\frac{\tilde{A}_z(k_x, y)}{J_0} = C_1 e^{-j\beta_0 y} + C_2 e^{j\beta_0 y} - \frac{\mu_0}{\beta_0} e^{jk_x x_0} \sin[\beta_0 (y - y_0)], \quad (2.11)$$

where

$$\beta_0 = \sqrt{k_0^2 - k_x^2}, \quad (2.12)$$

and C_1 and C_2 are the constants which are to be determined. According to the radiation condition, assuming imaginary part of the (2.12) smaller or equal to 0 ($\Im(\beta_0) \leq 0$) for $y \rightarrow \infty$, C_2 should be zero. Electrical field associated with magnetic vector potential is can be calculated as [14]:

$$\begin{aligned}\vec{E} &= -j\omega\vec{A} - j\frac{1}{\omega\mu\epsilon}\nabla(\nabla\cdot\vec{A}) \\ &= -j\omega J_0 \left\{ C_1 e^{-j\beta_0 y} - \frac{\mu_0}{\beta_0} e^{jk_x x_0} \sin[\beta_0(y-y_0)] \right\} \hat{z}.\end{aligned}\quad (2.13)$$

(2.13) should equal be zero for $y = 0$ so:

$$C_1 = \frac{\mu_0}{\beta_0} e^{jk_x x_0} \sin(\beta_0 y_0), \quad (2.14)$$

and re-arranging leads:

$$\begin{aligned}\tilde{A}_z(k_x, y) &= \frac{\mu_0}{\beta_0} J_0 e^{jk_x x_0} \left\{ \sin(\beta_0 y_0) e^{-j\beta_0 y} + \sin[\beta_0(y-y_0)] \right\} \\ &= \frac{\mu_0}{2j\beta_0} J_0 e^{jk_x x_0} \left\{ e^{-j\beta_0(y-y_0)} - e^{-j\beta_0(y+y_0)} + e^{j\beta_0(y-y_0)} - e^{-j\beta_0(y-y_0)} \right\},\end{aligned}\quad (2.15)$$

inverse Fourier transform of (2.15) is:

$$\begin{aligned}\hat{A}_z(x, y) &= -\frac{\mu_0}{4\pi} J_0 \int_{-\infty}^{\infty} \frac{1}{\beta_0} \left[e^{-j\beta_0(y+y_0)} - e^{j\beta_0(y-y_0)} \right] e^{-jk_x(x-x_0)} dk_x \\ &= \frac{\mu_0}{4j} J_0 \left[H_0^{(2)} \left(k_0 \sqrt{(x-x_0)^2 + (y-y_0)^2} \right) - H_0^{(2)} \left(k_0 \sqrt{(x-x_0)^2 + (y+y_0)^2} \right) \right].\end{aligned}\quad (2.16)$$

Scattered E-field is calculated from this vector potential as:

$$\vec{E}^s = -j\omega A_z \hat{z} = -\frac{k_0 \eta_0}{4} \hat{z} \int_C J(\vec{\rho}') G(\vec{\rho} | \vec{\rho}') dl', \quad (2.17)$$

where

$$G(\vec{\rho} | \vec{\rho}') = \left\{ H_0^{(2)} \left[k_0 \sqrt{(x-x')^2 + (y-y')^2} \right] - H_0^{(2)} \left[k_0 \sqrt{(x-x')^2 + (y+y')^2} \right] \right\} \quad (2.18)$$

and $\vec{\rho}$ is the observation point and $\vec{\rho}'$ is the source point:

$$\vec{\rho} = x\hat{x} + y\hat{y}, \vec{\rho}' = x'\hat{x} + y'\hat{y}. \quad (2.19)$$

Boundary condition on the bump surface C requires:

$$\vec{E}^i + \vec{E}^s = 0. \quad (2.20)$$

Solution for $J(\vec{\rho}')$ can be found using a Method of Moments scheme with point matching and pulse basis functions using equation (2.20). Bump can be represented with N linear segments as shown on Figure 2.3. Electrical current density can be approximated by pulse basis functions

$$\pi_n(\vec{\rho}) = \begin{cases} 1 & \vec{\rho} \text{ is on } C_n \\ 0 & \text{otherwise} \end{cases}, \quad (2.21)$$

where C_n denotes n^{th} linear segment on the bump, as

$$J(\vec{\rho}') = \hat{z} \sum_{n=1}^N J_n \pi_n(\vec{\rho}'). \quad (2.22)$$

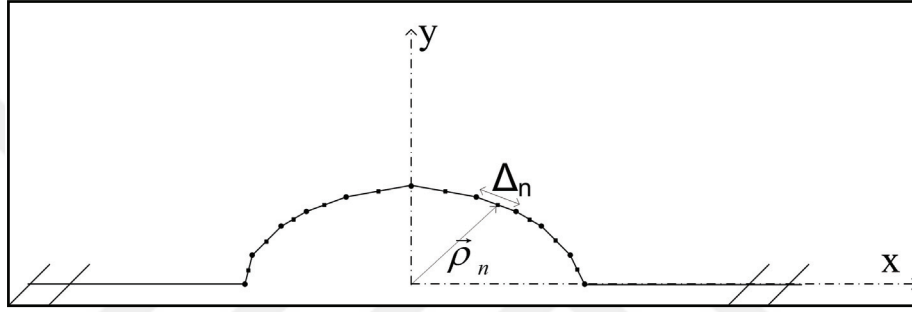


Figure 2.3 Linear segmentation on the cylindrical bump surface

Putting (2.22) into (2.20) yields

$$-\frac{k_0 \eta_0}{4} \hat{z} \sum_{n=1}^N J_n \int_C \pi_n(\vec{\rho}') G(\vec{\rho} | \vec{\rho}') dl' = -\vec{E}^i(\vec{\rho}). \quad (2.23)$$

Choosing $\vec{\rho}' = \vec{\rho}_n + \hat{I}_n l'$, where $\vec{\rho}_n$ is the center of the n^{th} segment and \hat{I}_n is the unit tangent vector of the n^{th} segment, (2.23) becomes

$$-\frac{k_0 \eta_0}{4} \hat{z} \sum_{n=1}^N J_n \int_{l'=-\Delta_n/2}^{\Delta_n/2} G(\vec{\rho} | \vec{\rho}_n) dl' = -\vec{E}^i(\vec{\rho}). \quad (2.24)$$

where Δ_n is the length of the n^{th} segment. Testing (2.24) with Dirac function $\delta(x-x_m)\delta(y-y_m)$,

$$-\frac{k_0 \eta_0}{4} \hat{z} \sum_{n=1}^N J_n \int_{l'=-\Delta_n/2}^{\Delta_n/2} \langle \delta(x-x_m)\delta(y-y_m), G(\vec{\rho} | \vec{\rho}_n) \rangle dl' = -\langle \delta(x-x_m)\delta(y-y_m), \vec{E}^i(\vec{\rho}) \rangle. \quad (2.25)$$

results in

$$\frac{k_0 \eta_0}{4} \hat{z} \sum_{n=1}^N J_n \int_{l'=-\Delta_n/2}^{\Delta_n/2} G(\bar{\rho}_m | \bar{\rho}_n) dl' = \bar{E}^i(\bar{\rho}_m). \quad (2.26)$$

Equation (2.26) can be written in matrix form as

$$[\alpha_{n,m}][J_n] = [E_m^i], \quad (2.27)$$

which can be solved by matrix inversion and multiplication. Here matrix elements are

$$\alpha_{n,m} = \frac{k_0 \eta_0}{4} \int_{-\Delta_n/2}^{\Delta_n/2} \left\{ \begin{array}{l} H_0^{(2)} \left[k_0 \sqrt{(x_m - x_n - I_{nx} l')^2 + (y_m - y_n - I_{ny} l')^2} \right] \\ -H_0^{(2)} \left[k_0 \sqrt{(x_m - x_n - I_{nx} l')^2 + (y_m + y_n + I_{ny} l')^2} \right] \end{array} \right\} dl'. \quad (2.28)$$

Scattered E-field can be calculated using J_n values as:

$$\bar{E}^s \cong \frac{k_0 \eta_0}{4} \sqrt{\frac{2j}{\pi k_0 \rho}} e^{-jk_0 \rho} \hat{z} \sum_{n=1}^N \Delta_n J_n e^{jk_0(x_n \cos \varphi + y_n \sin \varphi)} \quad (2.29)$$

where φ is the observation angle and ρ is the distance measured from origin to the observation point.

2.4 Solution by the Decomposition Method

If the discontinuity (cavity or bump) is absent, the calculation domain is free space for $y > 0$ and perfectly conducting for $y < 0$. The total Field is then

$$\bar{E}^{Total} = \begin{cases} \bar{E}^i + \bar{E}^{ref}(\bar{J}'_1) & y > 0 \\ 0 & y < 0 \end{cases} \quad (2.30)$$

Here, \bar{J}'_1 is the surface current density on an infinite perfectly conducting half space when illuminated by a plane wave. According to the boundary condition for the tangential electric field on the ground plane, current density on the ground plane can be calculated easily by

$$\bar{J}'_1 = 2\hat{y} \times \bar{H}^i = -\frac{2}{\eta_0} \sin \varphi^i e^{jk_0 x \cos \varphi^i} \hat{z}, \quad \text{on } S_1 \quad (2.31)$$

Here, η_0 is the intrinsic impedance of free space and \bar{H}^i is the magnetic field component of the incident plane wave on the ground plane.

In this manner, in the presence of the discontinuity there will be three additional different kinds of field components, \bar{E}^p , \bar{E}^{p1} , and \bar{E}^s . \bar{E}^p is the first type of

perturbated field corresponding to the effect of discontinuity on the ground plane; \vec{E}^{p1} is the second type of perturbated field due to the current density on the "vanished" region, as a result of the discontinuity ($x_1 < x < x_2$), shown on Figure 2.4; and \vec{E}^s is the field scattered from the discontinuity. The total fields on surfaces S_1 and S_2 are

$$\vec{E}^{Total} = \vec{E}^i + \vec{E}^{ref}(\vec{J}'_1) + \vec{E}^p(\vec{J}_1^p) + \vec{E}^s(\vec{J}_2) + \vec{E}^{p1}(\vec{J}_v) \quad (2.32)$$

Here, \vec{J}_2 is the electrical current density on the cylindrical discontinuity, \vec{J}_1^p is the induced perturbated current density on S_1 due to the discontinuity, and \vec{J}_v is the current density vanished due to the presence of the discontinuity, which is the negative of \vec{J}'_1 :

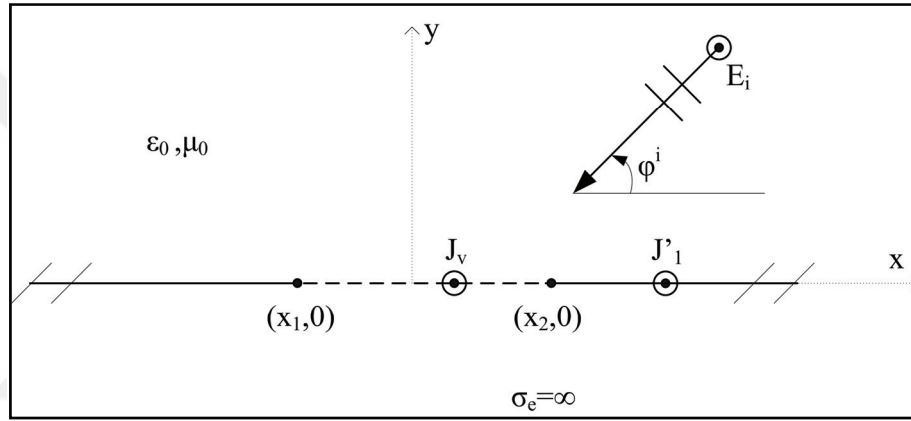


Figure 2.4 Demonstration of the vanished ground plane region

$$\vec{J}_v = -\vec{J}'_1, \quad y = 0, \quad x_1 < x < x_2 \quad (2.33)$$

On S_1 , $\vec{E}^i + \vec{E}^{ref}$ is zero according to the boundary condition and (2.30), so (2.32) becomes

$$\vec{E}^p(\vec{J}_1^p) + \vec{E}^s(\vec{J}_2) = -\vec{E}^{p1}(\vec{J}_v). \quad (2.34)$$

At this point, formulations for bump and indent problems deviate. For the cavity problem, owing to (2.30), the scatterer cross-section will be in the region $y < 0$ where there is not any incident or reflected fields when the cavity was absent. On the other hand, for the bump geometry, the scatterer cross-section will be in the region $y > 0$ where incident and the reflected fields exist. Thus, for the bump problem, the fields on S_2 satisfy

$$\vec{E}^p(\vec{J}_1^p) + \vec{E}^s(\vec{J}_2) = -\vec{E}^i - \vec{E}^{ref}(\vec{J}'_1) - \vec{E}^{p1}(\vec{J}_v), \quad (2.35)$$

and for the indent problem fields on S_2 satisfy

$$\vec{E}^p(\vec{J}_1^p) + \vec{E}^s(\vec{J}_2) = -\vec{E}^{p1}(\vec{J}_v). \quad (2.36)$$

After applying point matching with pulse basis functions, for the bump problem, a linear equation set is obtained in matrix form as

$$\begin{bmatrix} Z(k_0, \eta_0, S_1, S_1) & Z(k_0, \eta_0, S_2, S_1) \\ Z(k_0, \eta_0, S_1, S_2) & Z(k_0, \eta_0, S_2, S_2) \end{bmatrix} \begin{bmatrix} J_1^p \\ J_2 \end{bmatrix} = \begin{bmatrix} E^{p1}(k_0, S_1) \\ E^{t1}(k_0, S_2) \end{bmatrix}, \quad (2.37)$$

and for the indent problem as

$$\begin{bmatrix} Z(k_0, \eta_0, S_1, S_1) & Z(k_0, \eta_0, S_2, S_1) \\ Z(k_0, \eta_0, S_1, S_2) & Z(k_0, \eta_0, S_2, S_2) \end{bmatrix} \begin{bmatrix} J_1^p \\ J_2 \end{bmatrix} = \begin{bmatrix} E^{p1}(k_0, S_1) \\ E^{p1}(k_0, S_2) \end{bmatrix}, \quad (2.38)$$

where $Z(\cdot)$ operator is given as:

$$Z(k, \eta, S_n, S_m) = \frac{k\eta}{4} \int_{l'=-\Delta_n/2}^{\Delta_n/2} H_0^{(2)}\left(k \left\| \vec{\rho}_m - (\vec{\rho}_n + l' \hat{I}_n) \right\| \right) dl', \quad (2.39)$$

Derivation and calculation of the self-terms ($\vec{\rho}_n \rightarrow \vec{\rho}_m$) of (2.39) are can be found on appendix A. Using (2.31), the pertubated field excited by the “vanished” current density J_v is

$$\begin{aligned} E^{p1}(k, S_m) &= \frac{k\eta}{4} \int_{x_1}^{x_2} J_v(x') H_0^{(2)}\left(k \sqrt{(x_m - x')^2 - y_m^2}\right) dx' \\ &= \frac{k}{2} \sin \varphi^i \int_{x_1}^{x_2} e^{jkx' \cos \varphi^i} H_0^{(2)}\left(k \sqrt{(x_m - x')^2 - y_m^2}\right) dx', \end{aligned} \quad (2.40)$$

and

$$E^{t1}(k, S_m) = E^i + E^{ref} + E^{p1}(k, S_m) = 2j e^{jkx_m \cos \varphi^i} \sin(ky_m \sin \varphi^i) + E^{p1}(k, S_m). \quad (2.41)$$

The unknown current densities J_1^p and J_2 are calculated by solving the matrix equations of (2.37) or (2.38). Calculation of the integrals on equations (2.39) and (2.40) can be performed numerically. The scattered field is calculated by using far-field approximations:

$$\begin{aligned} \vec{E}^s &\cong \frac{k_0 \eta_0}{4} \sqrt{\frac{2j}{\pi k_0 \rho}} e^{-jk_0 \rho} \left[\sum_{i=1}^{N_1} \Delta_i (J_1^p)_i e^{jk_0(x_i \cos \varphi + y_i \sin \varphi)} + \sum_{l=1}^{N_2} \Delta_l (J_2)_l e^{jk_0(x_l \cos \varphi + y_l \sin \varphi)} \right] \hat{z} \\ &- j \sqrt{\frac{2j}{\pi k_0 \rho}} e^{-jk_0 \rho} \frac{\sin \varphi^i}{\cos \varphi^i + \cos \varphi} \left[e^{jk_0(\cos \varphi^i + \cos \varphi)x_1} - e^{jk_0(\cos \varphi^i + \cos \varphi)x_2} \right] \hat{z} \end{aligned} \quad (2.42)$$

Here, N_1 and N_2 are the number of linear segments on S_1 and S_2 respectively. The last term on (2.42) is derived from equation (2.40) using far field approximations, which is the field excited by J_v . Scattering width in terms of scattered and incident fields is defined as:

$$\sigma = \lim_{\rho \rightarrow \infty} \left[2\pi\rho \left| \frac{E^s}{E^i} \right| \right] \quad (2.43)$$

2.5 Numerical Results

In order to show the validity of the method, the monostatic scattering width of a semi-circular bump with $k_0a = 2\pi$ on Figure 2.5 is compared with the series solution result given on section 2.2. The perturbation current calculation domain length is chosen as $l = 5\lambda + 2a$, where a is the bump radius and λ is the free space wavelength corresponding to the calculation frequency.

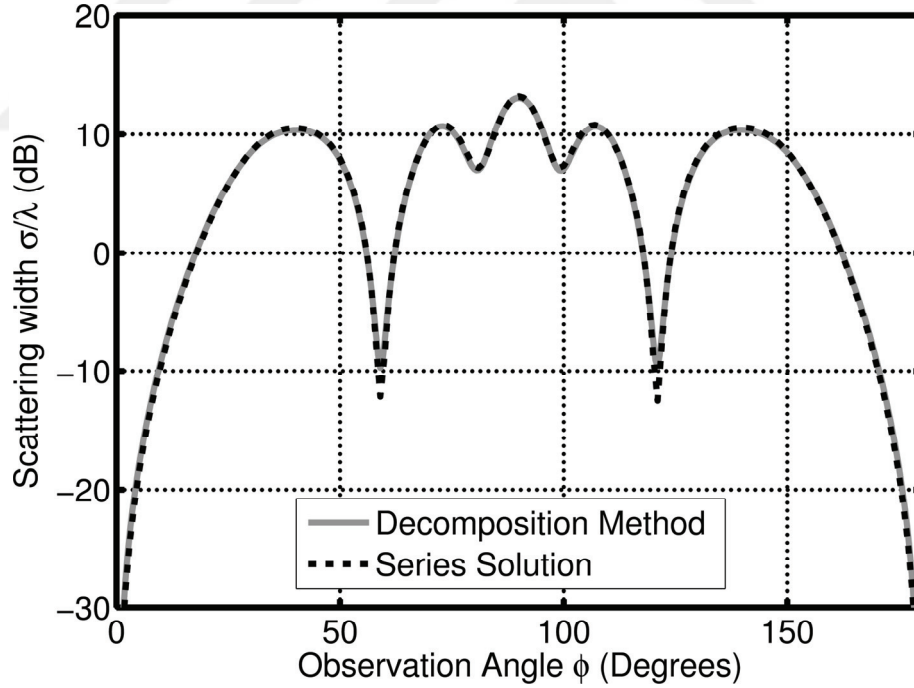


Figure 2.5 Monostatic scattering width of a semi-circular bump with a radius of λ

As can be seen in Figure 2.5, the results are in near excellent agreement.

Afterwards the convergence of the solution with the change of the strip width l is investigated, and results are shown in Figure 2.6 as mean error ratio of current and error

ratio for far-field results at observation angle $\varphi = 90^\circ$, compared to the reference MoM solution given on section 2.3 for $k_0 a = \pi$ in the vicinity of normal ($\varphi^i = 90^\circ$) plane wave incidence. Both results converge to the numerical error level while l approaches 2.5. At this point it should be noted that proper selection of l is should not only be dependent on wavelength but also on scatterer size. Both current densities are presented also in Figure 2.7 which are calculated at 300 MHz and a semi-circular bump with radius of 1 m. Mean error ratio for current density is calculated as:

$$\text{Error} = E \left[\frac{|J^{dec} - J^{MoM}|}{|J^{MoM}|} \right], \quad (2.33)$$

and the far-field error is calculated as:

$$\text{Error} = \frac{|E^{dec} - E^{MoM}|}{|E^{MoM}|} \quad (2.34)$$

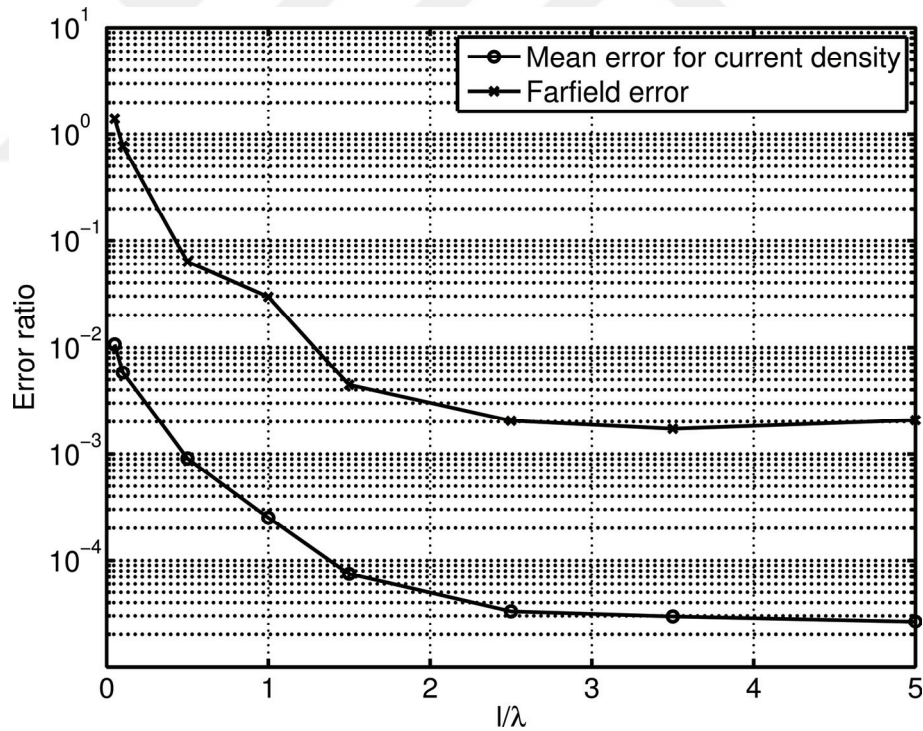


Figure 2.6 Convergence of the solution with strip length l

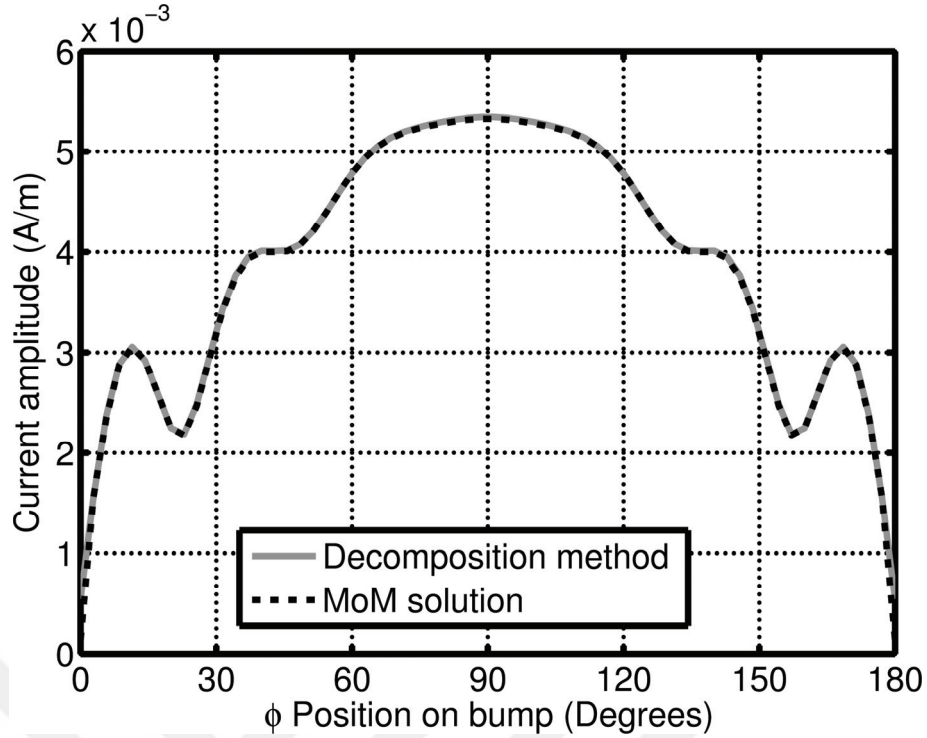


Figure 2.7 Current distribution comparison for $l / \lambda = 5$

Here, J^{dec} and J^{MoM} are current densities on the circular bump calculated by Decomposition method and MoM, respectively; E^{dec} and E^{MoM} are scattered field calculated by two methods; and $E[\cdot]$ is the mean value operator.

Monostatic scattering width of a triangular bump, shown in Figure 2.8 versus observation angle, is presented on Figure 2.9 for the MoM solution. The bump has a base width of 8λ and a height of 2λ .

Results are almost identical except around 20° and 160° . Peaks around 60° and 120° correspond to specular reflections from the flat surfaces of the bump.

Backscattered scattering cross length for semicircular cavity in a perfectly conducting ground plane with $k_0 a = 4\pi$ is shown in Figure 2.10 with the result from [15]. Reference and calculated results are nearly indistinguishable, and it is thought that errors made during data extraction from the reference article may have caused the small deviations seen.

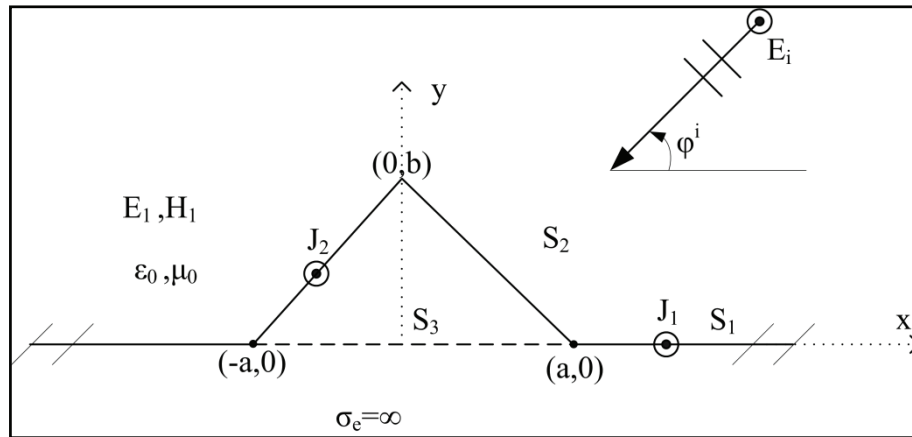


Figure 2.8 Triangular bump geometry

Next, the semi-elliptical cavity in a ground plane geometry depicted in Figure 2.11 is investigated for different eccentricity values which is related to the dimensions a and b with the expression $b = a\sqrt{1-e^2}$. The backscattered normalized field [16] versus k_0a is compared with results of [16] in Figure 2.12. Again, the results agree very well, except for minor offset error along the k_0a axis, which is due to data extraction.

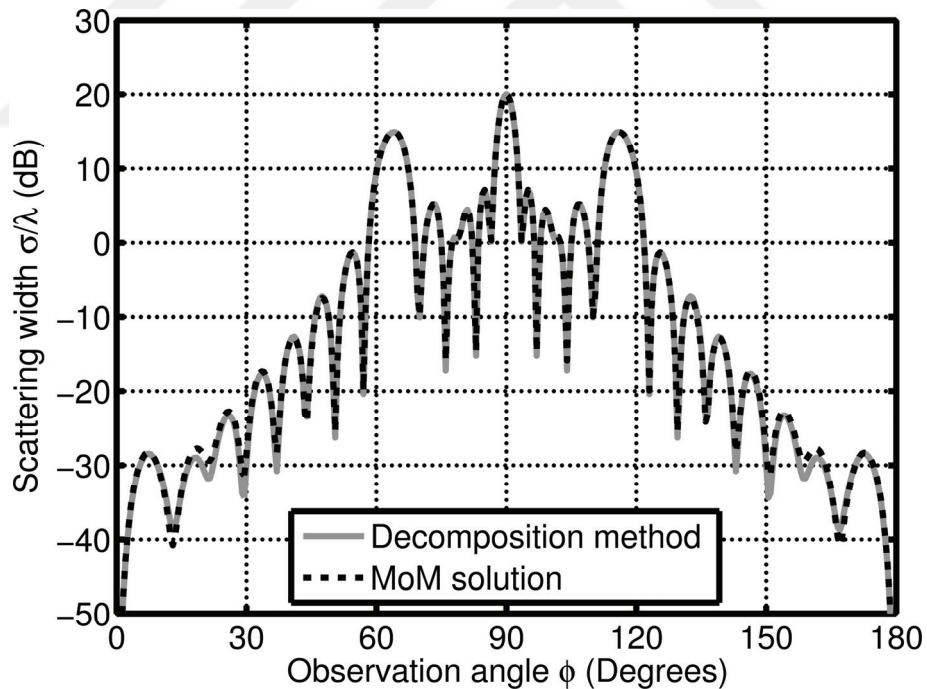


Figure 2.9 Monostatic scattering width of a triangular bump

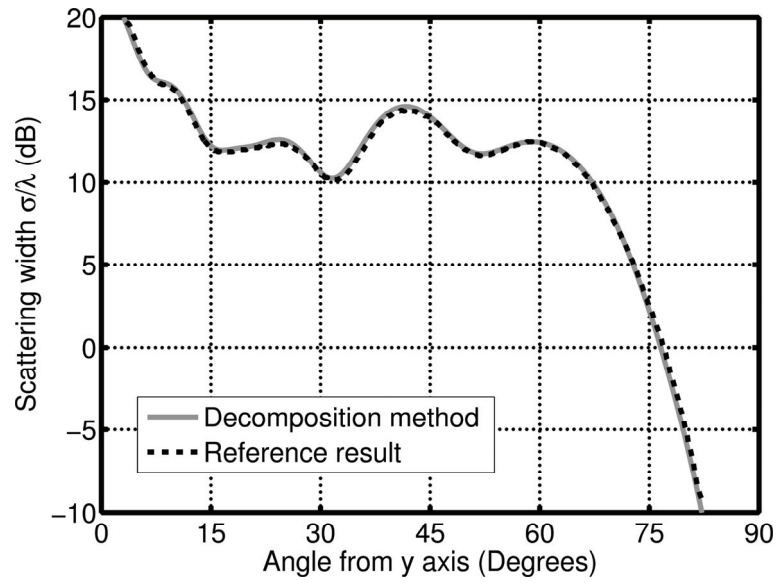


Figure 2.10 Calculation results for the semi-circular cavity

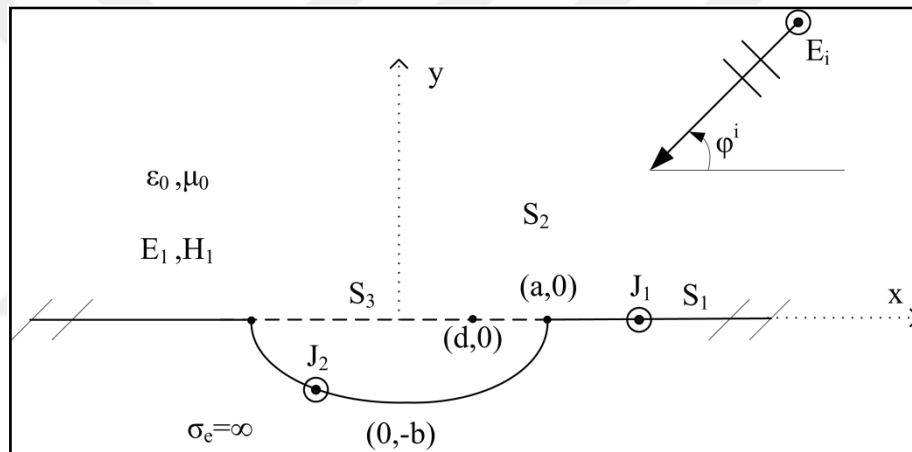


Figure 2.11 Semi-elliptical cavity geometry

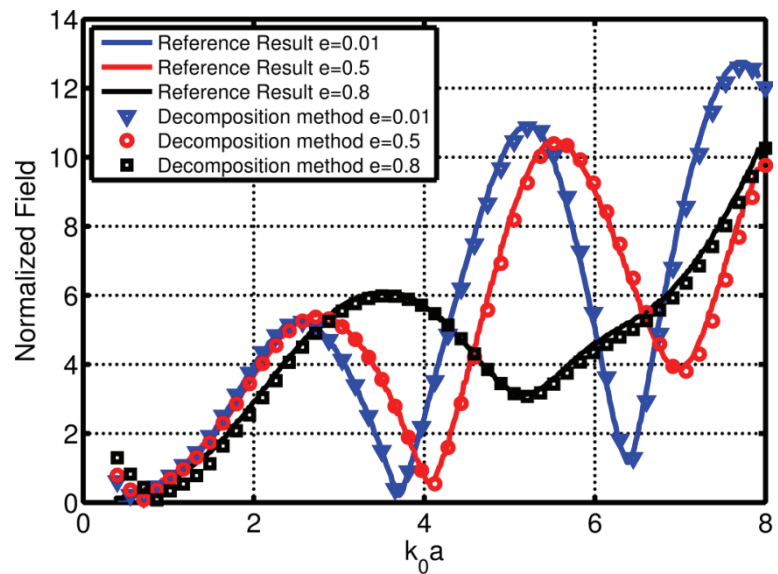


Figure 2.12 Calculation results for the semi-elliptical cavity

Lastly, rectangular and triangular cavity geometries shown in Figure 2.13 are examined and simulation results are compared with reference publications [17] and [18] in Figure 2.14. For the rectangular geometry, a and b values are 0.6λ and 0.8λ , respectively, and for the triangular geometry a and b are 0.75λ and 1.65λ .

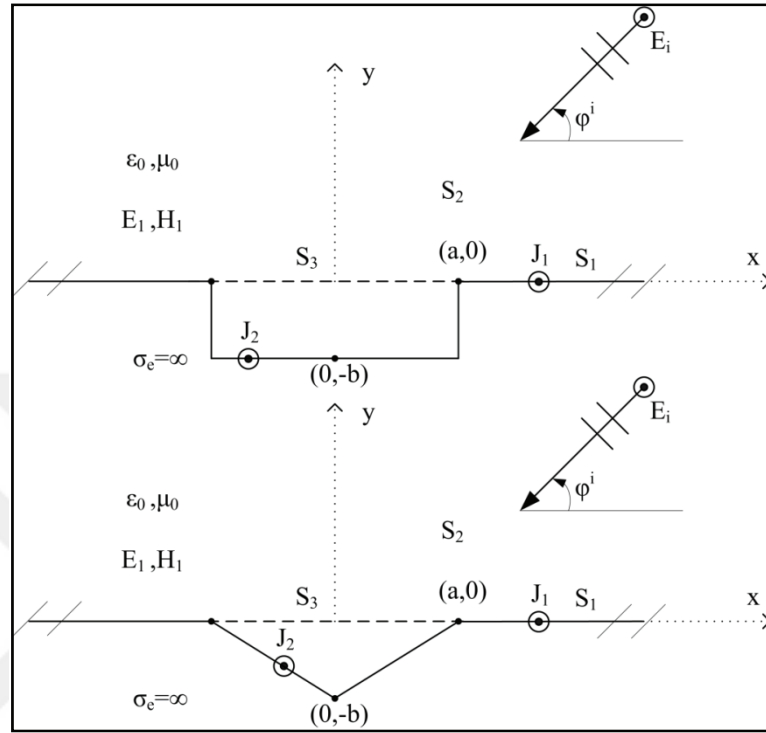


Figure 2.13 The rectangular and triangular cavities

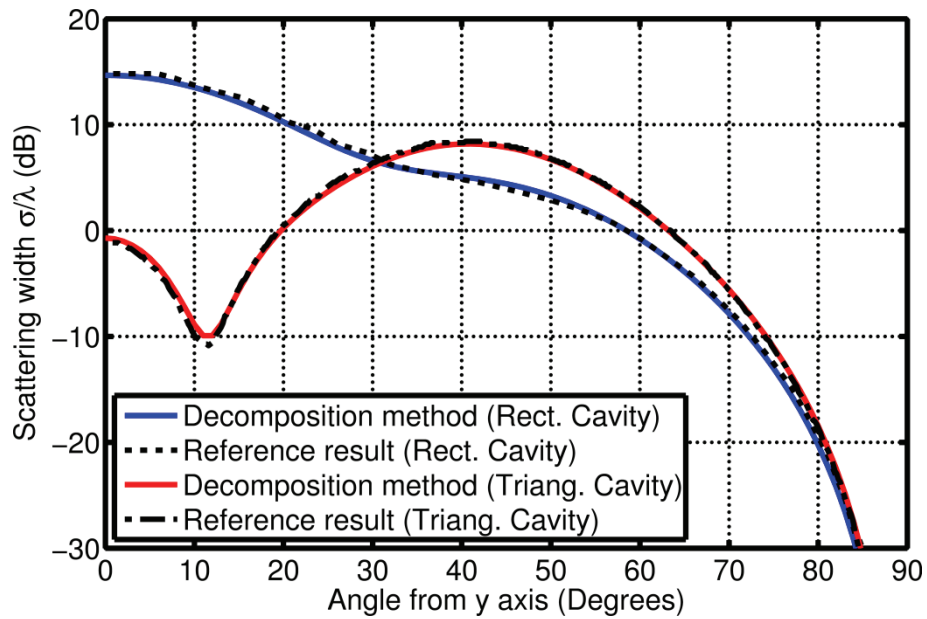


Figure 2.14 Calculation results for the rectangular and triangular cavities

SCATTERING FROM AN OVERFILLED CYLINDRICAL CAVITY ON A PERFECTLY CONDUCTING INFINITE GROUND PLANE

3.1 Introduction

In this chapter, plane wave scattering from an overfilled cavity is presented. First, a brief summary of the literature work dealing with this problem is introduced. Afterwards solution of the problem by the decomposition method is introduced. Lastly, numerical solutions are presented with examples from the literature for validation purposes.

Scattering problem is a two-dimensional overfilled cavity, which has a dielectric permittivity of ϵ_1 , magnetic permeability of μ_1 and electrical conductivity of σ_{e1} embedded in a PEC ground plane. The cavity with arbitrary cross section is defined by surfaces S_2 and S_3 , depicted on Figure 3.1, where S_2 is in the upper half-space ($y > 0$) and S_3 is in the lower half-space ($y < 0$).

Problem is an arbitrary bump on an infinite perfectly conducting ground plane if electrical conductivity σ_{e1} of the region 2 is chosen as infinite and an indent (or cavity) if medium parameters of the region 2 is chosen to be free space. So both these type of problems, which are considered in Chapter 2, can be solved by solving the overfilled cavity problem.

A TM_z polarized plane wave with electric field component given on (2.1) is incident on the cavity with the incidence angle φ^i .

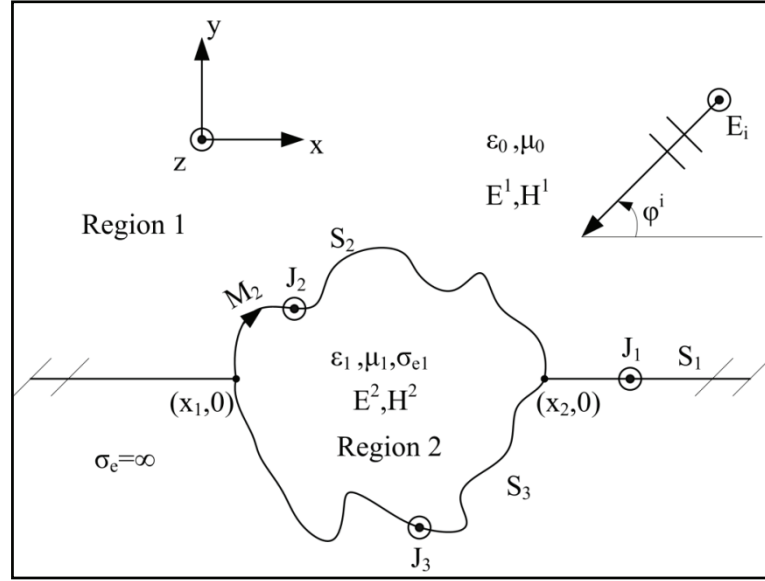


Figure 3.1 Scattering geometry

3.2 Literature

Works dealing with these problems are available in the literature; solution methods include analytical solutions [16], [19]-[21] for canonical structures. For example, Byun et al. [16] solved scattering from an overfilled cavity with elliptical cross section with a series solution and Kolbehdari et al. [21] solved scattering from an overfilled cavity with a circular cross section analytically by using equivalency principle. Arancibia and Bruno's paper [22] includes a solution to this problem and Wood published a paper [23] involving this problem.

3.3 Solution by the Decomposition Method

Solution begins with the case when the overfilled cavity is not present. Total field for $y > 0$ would be the summation of incident (\vec{E}^i) and reflected field ($\vec{E}^{ref}(\vec{J}'_1)$) from the infinite ground plane as given on (2.19). In the presence of the overfilled cavity, using surface equivalence principle, the problem can be decomposed into two parts, which are the upper equivalency for region 1 and the internal equivalency for the region 2 as shown in Figure 3.2. At this point, an electrical current density \vec{J}_1^p is introduced on the surface S_1 , near the cavity, which will be called "perturbated electrical current density", which is assumed to be rapidly decaying away from the cavity. Therefore, the total current density \vec{J}_1 on S_1 is the superposition of \vec{J}_1^p and \vec{J}'_1 .

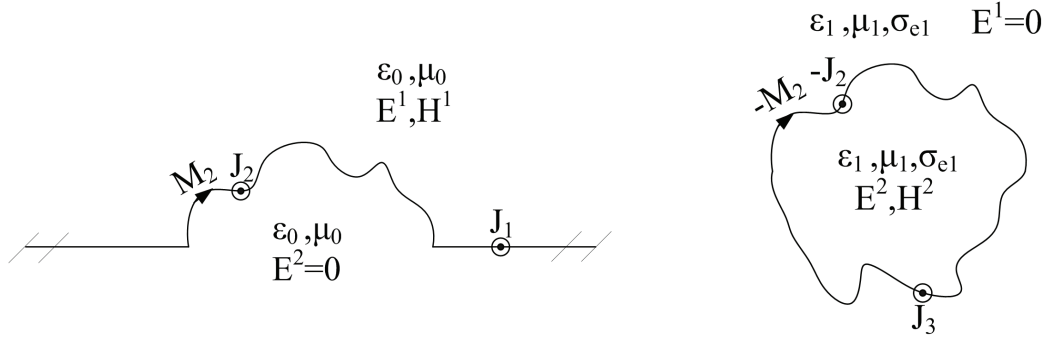


Figure 3.2 Application of the equivalency principle on the scatterer, (a) upper equivalence, (b) internal equivalence

The total E-field in region 1 for the upper equivalence region is

$$\vec{E}^1 = \vec{E}^i + \vec{E}^{ref}(\vec{J}'_1) + \vec{E}^p(\vec{J}_1^p) + \vec{E}^s(\vec{J}_2, \vec{M}_2) + \vec{E}^{p1}(\vec{J}_v). \quad (3.1)$$

Here, \vec{J}_2 and \vec{M}_2 are the equivalent electric and magnetic current densities on S_2 .

According to the boundary condition of vanishing tangential component of the total E-field on PEC surface, $\vec{E}^i + \vec{E}^{ref}$ is zero on S_1 so (3.1) becomes:

$$\vec{E}^p(\vec{J}_1^p) + \vec{E}^s(\vec{J}_2, \vec{M}_2) = -\vec{E}^{p1}(\vec{J}_v), \quad (3.2)$$

and on S_2 electrical field satisfy:

$$\vec{E}^p(\vec{J}_1^p) + \vec{E}^s(\vec{J}_2, \vec{M}_2) = -[\vec{E}^i + \vec{E}^{ref}(\vec{J}'_1) + \vec{E}^{p1}(\vec{J}_v)] = \vec{E}^{t1}, \quad (3.3)$$

where \vec{E}^{t1} is the total field on S_2 . On the other hand, the total E-field in region 2 for the internal equivalence region is

$$\vec{E}^2 = \vec{E}^s(-\vec{J}_2, -\vec{M}_2) + \vec{E}^s(\vec{J}_3). \quad (3.4)$$

Electrical fields satisfy boundary condition:

$$\vec{E}^s(-\vec{J}_2, -\vec{M}_2) + \vec{E}^s(\vec{J}_3) = 0, \quad (3.5)$$

on S_2 and S_3 , where \vec{J}_3 is the electrical current density on S_3 . Negative signs on equations (3.3) and (3.4) are due to the equivalency principle. After applying a MoM scheme based on pulse basis functions and point matching, the equations (3.2), (3.3) and (3.5) become a set of linear equations and written in matrix form as

$$\begin{bmatrix} Z(k_0, \eta_0, S_1, S_1) & Z(k_0, \eta_0, S_1, S_2) & K(k_0, S_1, S_2) & [0] \\ Z(k_0, \eta_0, S_2, S_1) & Z(k_0, \eta_0, S_2, S_2) & K(k_0, S_2, S_2) & [0] \\ [0] & Z(k_1, \eta_1, S_2, S_2) & K(k_1, S_1, S_2) & Z(k_1, \eta_1, S_2, S_3) \\ [0] & Z(k_1, \eta_1, S_3, S_2) & K(k_1, S_3, S_2) & Z(k_1, \eta_1, S_3, S_3) \end{bmatrix} \begin{bmatrix} J_1^p \\ J_2 \\ M_2 \\ J_3 \end{bmatrix} = \begin{bmatrix} E^{p1}(k_0, S_1) \\ E^{t1}(k_0, S_2) \\ [0] \\ [0] \end{bmatrix}. \quad (3.6)$$

Here, matrix elements are given by (2.28) and:

$$K(k, S_m, S_n) = \frac{jk}{4} \int_{l'=-\Delta_n/2}^{\Delta_n/2} H_1^{(2)}\left(k \left\| \vec{\rho}_m - (\vec{\rho}_n + l' \hat{I}_n) \right\| \right) \frac{\hat{n}_n \cdot (\vec{\rho}_n - \vec{\rho}_m)}{\left\| \vec{\rho}_m - (\vec{\rho}_n + l' \hat{I}_n) \right\|} dl'. \quad (3.7)$$

Calculation of the self-terms ($\vec{\rho}_n \rightarrow \vec{\rho}_m$) of the equation (3.7) are can be found on Appendix A.

The terms E^{p1} and E^{t1} on right hand side of the (3.6) can be calculated by equations (2.29) and (2.30). Current densities, J_1^p , J_2 , M_2 , and J_3 can be calculated by solving the matrix equation (3.6). Thereafter, the scattered electric field in region 1 can be calculated approximately using J_1^p , J_2 , M_2 , and J_v with far field approximations:

$$\begin{aligned} \vec{E}^s &\cong \frac{k_0 \eta_0}{4} \sqrt{\frac{2j}{\pi k_0 \rho}} e^{-jk_0 \rho} \begin{bmatrix} \sum_{i=1}^{N_1} \Delta_i (J_1^p)_i e^{jk_0(x_i \cos \varphi + y_i \sin \varphi)} \\ + \sum_{l=1}^{N_2} \Delta_l (J_2)_l e^{jk_0(x_l \cos \varphi + y_l \sin \varphi)} \end{bmatrix} \hat{z} \\ &- \frac{k_0}{4} \sqrt{\frac{2j}{\pi k_0 \rho}} e^{-jk_0 \rho} \sum_{h=1}^{N_2} (-\cos \varphi \hat{y} + \sin \varphi \hat{x}) \cdot \hat{I}_h \Delta_h (M_2)_h e^{jk_0(x_h \cos \varphi + y_h \sin \varphi)} \hat{z} \\ &- j \sqrt{\frac{2j}{\pi k_0 \rho}} e^{-jk_0 \rho} \frac{\sin \varphi^i}{\cos \varphi^i + \cos \varphi} \left[e^{jk_0(\cos \varphi^i + \cos \varphi)x_1} - e^{jk_0(\cos \varphi^i + \cos \varphi)x_2} \right] \hat{z} \end{aligned} \quad (3.8)$$

Similarly, fields in region 2 can be calculated using J_2 , M_2 and J_3 .

3.4 Numerical Results

In order to verify validity of the method, several scattering scenarios are considered in this section. Calculations are performed by selecting strip length l as $5\lambda + d$, which is found to be an appropriate choice on [24], where d is the maximum dimension of the scatterer.

In order to compare with the series solution, first, a PEC semicircular bump on a PEC ground plane is investigated. Surfaces S_2 and S_3 are circular (in this case shape of S_3 is not effecting the results because it is in the PEC half-space), together forming a circle with radius λ , region 1 is free space and region 2 has almost infinite electrical

conductivity ($\sigma_{e2} \rightarrow \infty$). Monostatic scattering width versus observation angle is presented on Figure 3.3 and compared with the series solution given on (2.8) and perturbed current density amplitude distribution on the ground plane is given as an example at Figure 3.4 for different incidence angles.

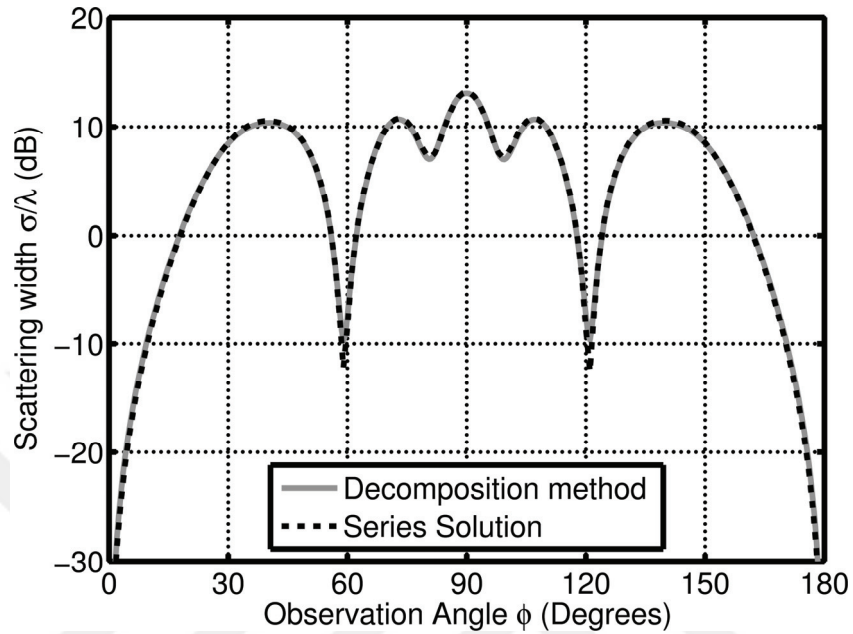


Figure 3.3 Scattering width of a semicircular bump with radius λ on an infinite perfectly conducting ground plane

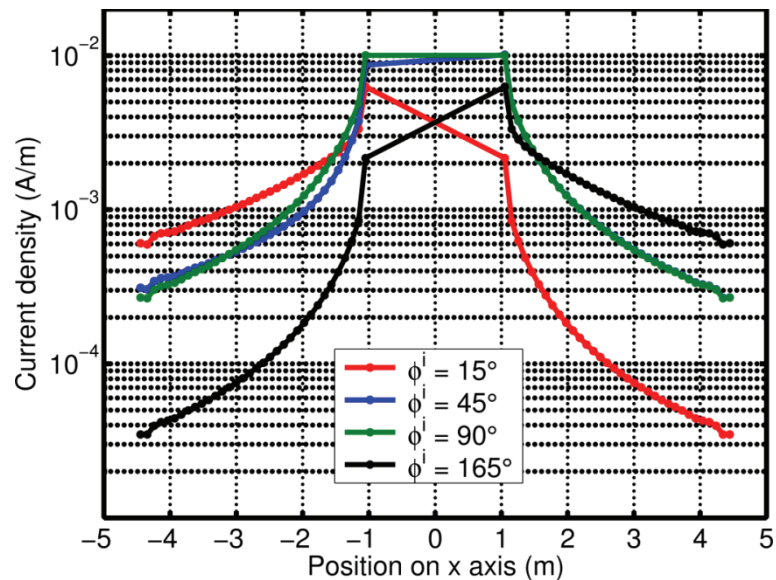


Figure 3.4 Perturbed current density on S_1 for various incidence angles

It can be seen that results are almost identical, and scattering width approaches zero when observation angle approaches grazing angles 0° and 180° as expected for this

polarization and configuration. On the other hand, it should be noted that the perturbed current densities on Figure 3.4 for $\varphi^i = 15^\circ$ and 165° are symmetrical with respect to vertical axis and current densities rapidly vanishes away with distance, again as expected.

Secondly, a triangular empty cavity in a PEC ground plane shown on Figure 3.5 is examined. Here, S_2 is circular and S_3 is triangular (in this case shape of S_2 is not effecting the results) with a and b are 0.75λ and 1.65λ , respectively. Also, region 1 and region 2 are free space. Monostatic scattering width versus observation angle is presented on Figure 3.6 compared with the reference solution given on [18].

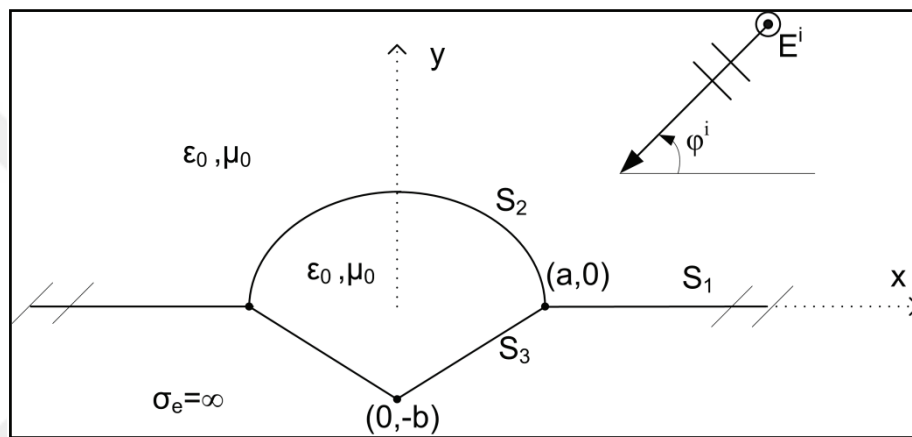


Figure 3.5 Geometry for scattering by a triangular cavity in an infinite ground plane

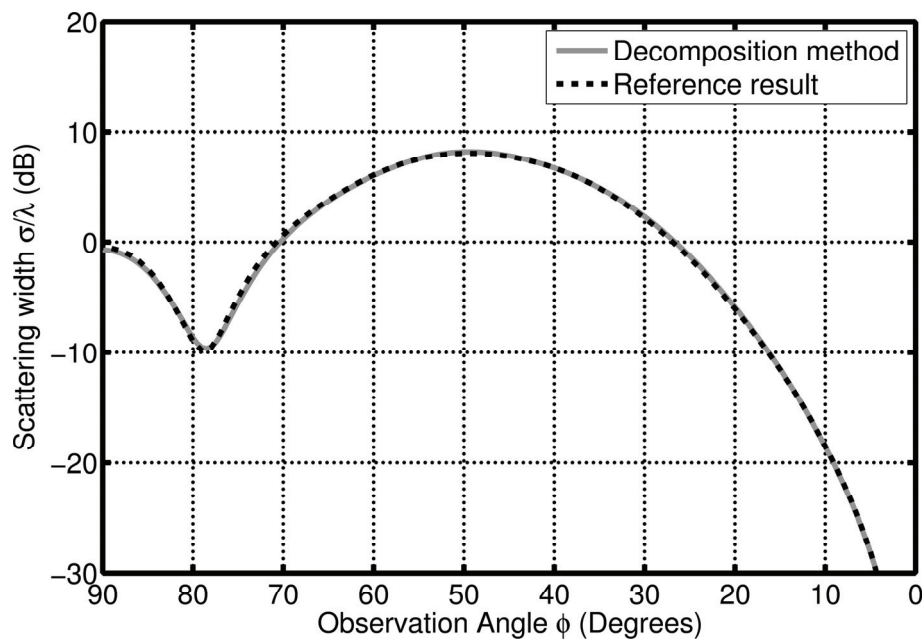


Figure 3.6 Results for scattering by a triangular cavity in an infinite ground plane

Afterwards, scattering from an overfilled cavity with elliptical cross section embedded in an infinitely-long PEC ground plane shown on Figure 3.7 is examined. Here, the elliptical cavity with dimensions a and b is defined by S_2 and S_3 surfaces. The cross section dimensions a and b are related to the eccentricity value e with the expression $b = a\sqrt{1-e^2}$. Region 1 is free space and region 2 has a relative dielectric permittivity of $\epsilon_r = 3$ and magnetic permeability of $\mu_r = 1$, the incidence angle is chosen to be $\phi^i = 90^\circ$.

Monostatic normalized scattered field amplitudes [16] versus $k_0 a$ is presented on Figure 3.8 with the reference analytical solution given in [16].

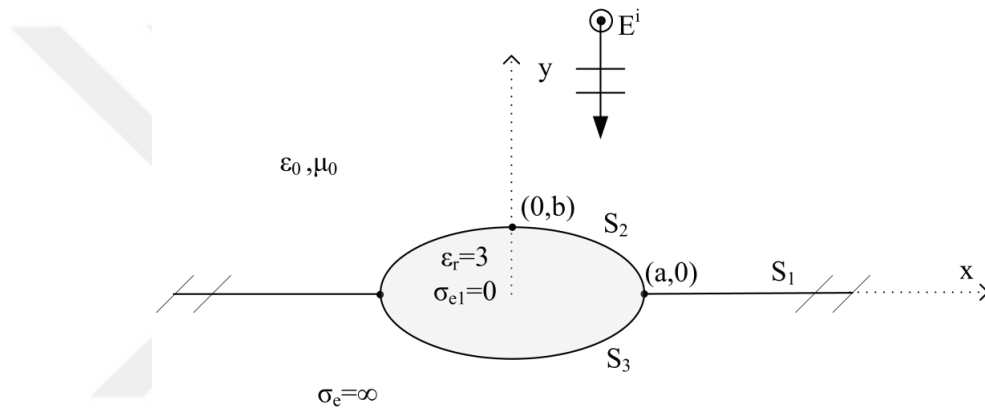


Figure 3.7 Scattering geometry for monostatic scattering by a material loaded elliptical cavity in an infinite ground plane

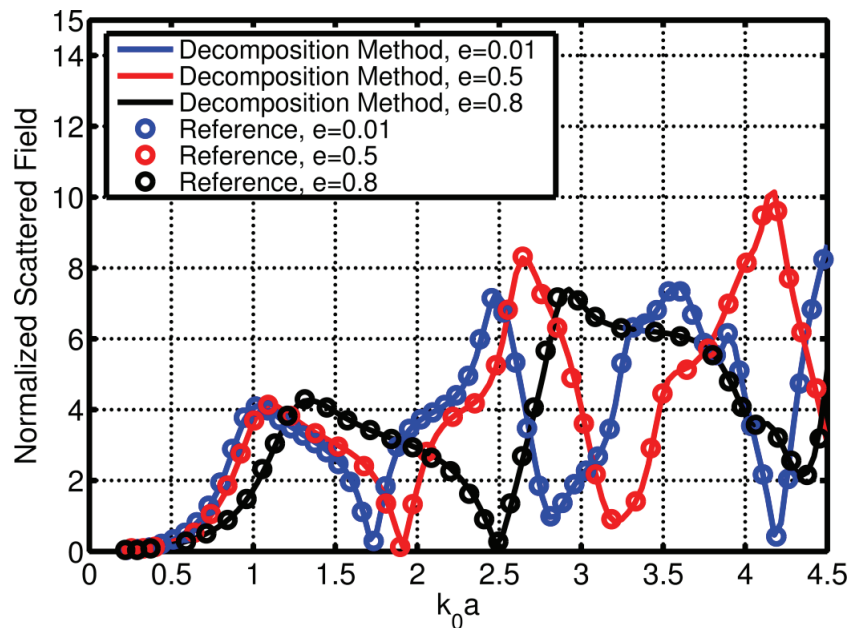


Figure 3.8 Results for monostatic scattering by a material loaded cavity in an infinite ground plane

Then, bistatic scattering results for an overfilled cavity with elliptical cross section embedded in an infinitely long PEC ground plane is shown on Figure 3.9 for $k_0 a = 2\pi$ with different relative dielectric permittivity and eccentricity values are represented on Figure 3.10 with reference results [16]. In this scenario, a plane wave is incident on the overfilled elliptical cavity with an angle of $\varphi^i = 60^\circ$.

Generally, the results agree very well with the results in [16] except that the minor deviations in the result for $\epsilon_r = 4$ and $e = 0.01$ which is thought to be due to the errors made during extraction of data from the reference paper.

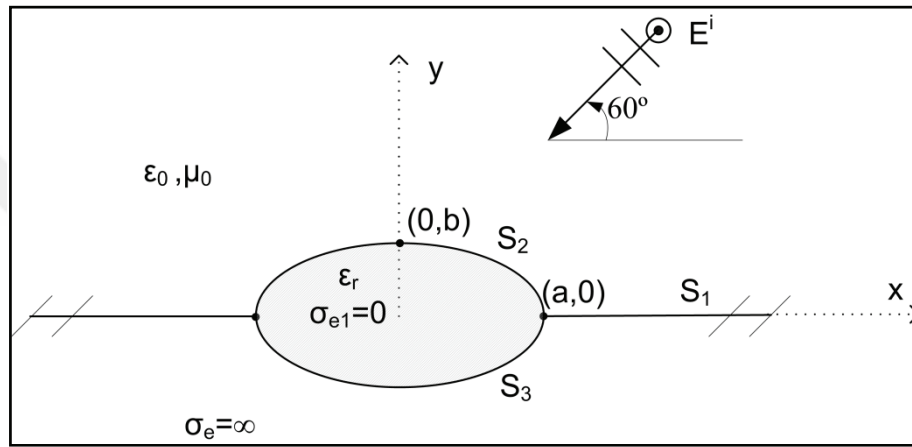


Figure 3.9 Scattering geometry for bistatic scattering by a material loaded elliptical cavity in an infinite ground plane

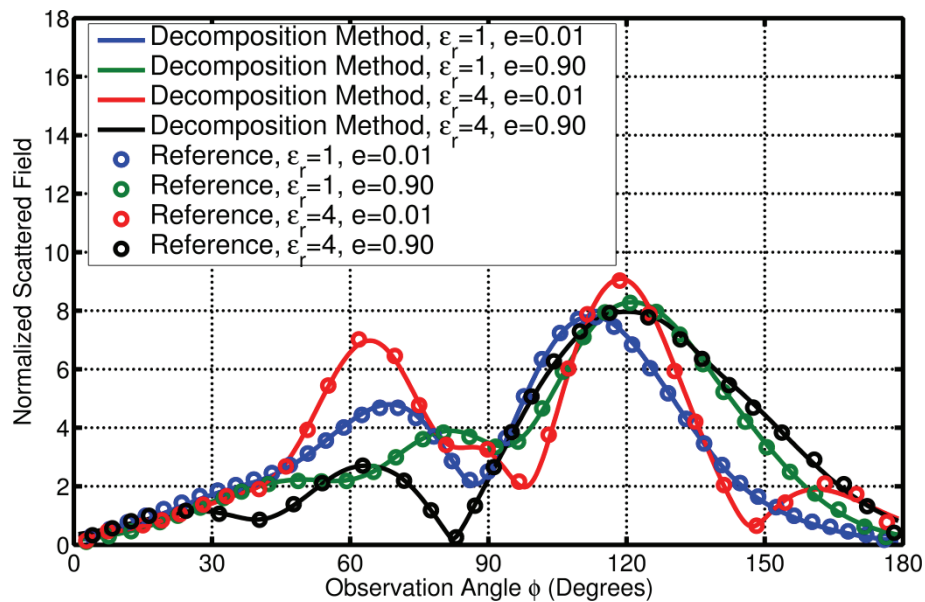


Figure 3.10 Results for bistatic scattering by a material loaded cavity in an infinite ground plane

Finally, monostatic scattering from a circular cavity filled with lossy dielectric material is analyzed and presented on Figure 3.11 for different conductivity values with normal incidence, versus $k_0 a$. Lossless case on Figure 3.11 is approximately equal to the case for $e = 0.01$ on Figure 3.8. Series solution for a perfectly conducting semicircular bump given on (2.8) which corresponds to the highly conducting case (red curve) is added to the figure for comparison.

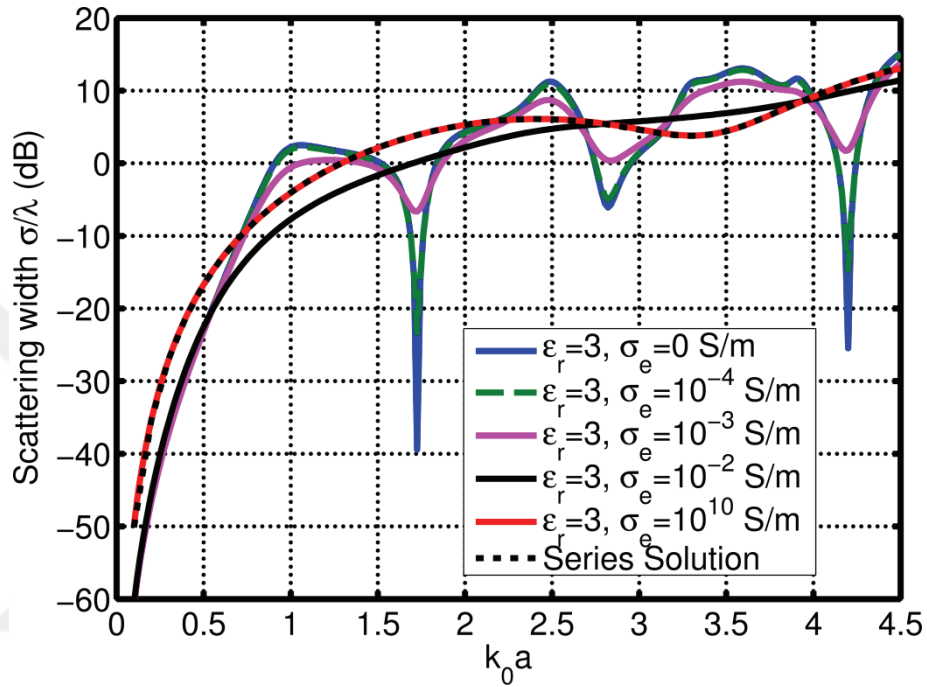


Figure 3.11 Results for monostatic scattering by a lossy material loaded cavity on an infinite ground plane

As can be seen on Figure 3.11, as conductivity value increases, resonant behavior of the scattering geometry ceases to exist and result for the case, which $\sigma_{el} = 10^{10}$ is identical to the series solution.

SCATTERING FROM A PERFECTLY CONDUCTING
CYLINDER PARTIALLY BURIED IN A DIELECTRIC HALF
SPACE

4.1 Introduction

In this chapter, solution of plane wave scattering from a perfectly conducting cylinder with arbitrary cross section partially buried in a material half-space with decomposition method is presented with example scattering scenarios.

Scattering problem is a two-dimensional perfectly conducting object, which is partially buried in a dielectric half space which has a dielectric permittivity of ϵ_2 , magnetic permeability of μ_2 and electrical conductivity of σ_{e2} . The object with arbitrary cross section is defined by surfaces S_2 and S_3 , depicted on Figure 4.1, where S_2 is in the upper half-space ($y > 0$) and S_3 is in the lower half-space ($y < 0$).

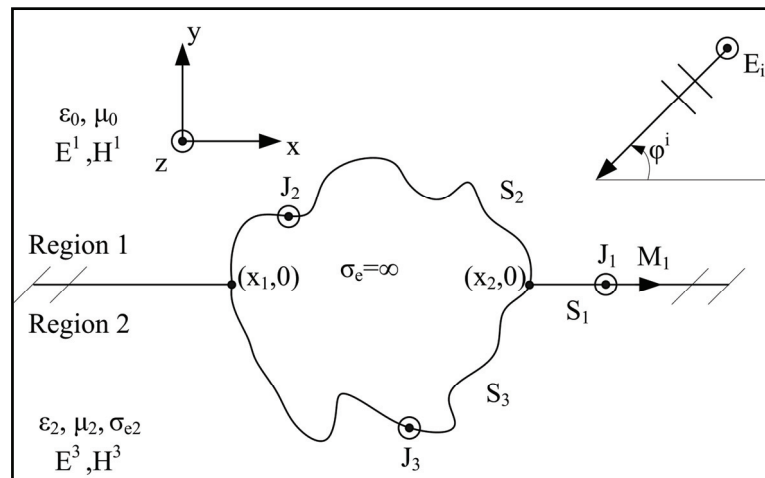


Figure 4.1 Scattering geometry

A TM_z polarized plane wave with electric field component given on (2.1) is incident on the object with the incidence angle φ^i .

4.2 Solution by the Decomposition Method

If the scattering object was not present, total field would be summation of incident and reflected fields for $y > 0$ and transmitted field for $y < 0$:

$$\vec{E}^{Total} = \begin{cases} \vec{E}^i + \vec{E}^{ref}(\vec{J}'_1, \vec{M}'_1) & y > 0 \\ \vec{E}^{trans}(\vec{J}'_1, \vec{M}'_1) & y < 0 \end{cases} \quad (4.1)$$

where \vec{E}^i is given by (2.1), \vec{E}^{ref} is given by [14]:

$$\vec{E}^{ref} = \Gamma e^{jk_0(x \cos \varphi^i - y \sin \varphi^i)} \hat{z}, \quad (4.2)$$

and \vec{E}^{trans} is given by

$$\vec{E}^{trans} = (1 + \Gamma) e^{jk_2(x \cos \varphi^i + y \sin \varphi^i)} \hat{z}, \quad (4.3)$$

and

$$\vec{J}'_1 = \begin{cases} \hat{y} \times \vec{H}_1 = \hat{z} \frac{1}{\eta_0} [1 - \Gamma] \sin \varphi^i e^{jk_0 x \cos \varphi^i}, & y \rightarrow 0^+ \\ \hat{y} \times \vec{H}_2 = -\hat{z} \frac{1}{\eta_2} [1 + \Gamma] \sin \varphi^i e^{jk_2 x \cos \varphi^i}, & y \rightarrow 0^- \end{cases}, \quad (4.4)$$

and

$$\vec{M}'_1 = - \begin{cases} \hat{y} \times \vec{E}_1, & y \rightarrow 0^+ \\ \hat{y} \times \vec{E}_2, & y \rightarrow 0^- \end{cases} = -[1 + \Gamma] \hat{x} \begin{cases} e^{jk_0 x \cos \varphi^i}, & y \rightarrow 0^+ \\ -e^{jk_2 x \cos \varphi^i}, & y \rightarrow 0^- \end{cases}. \quad (4.5)$$

Where the reflection coefficient Γ is

$$\Gamma = \frac{\eta_2 \cos \varphi^i - \eta_0 \cos \varphi^t}{\eta_2 \cos \varphi^i + \eta_0 \cos \varphi^t}, \quad (4.6)$$

and

$$\varphi^t = \arcsin \left(\frac{k_0}{k_2} \sin \varphi^i \right). \quad (4.7)$$

In the presence of the object, using surface equivalence principle, the problem can be decomposed into two parts, which are the upper equivalency for region 1 and the lower equivalency for the region 2 as shown in Figure 4.2. At this point, electrical and

magnetic current densities \vec{J}_1^p , \vec{M}_1^p are introduced on the surface S_1 , near the object.

Therefore, the total current densities \vec{J}_1 and \vec{M}_1 on S_1 are:

$$\vec{J}_1 = \vec{J}_1' + \vec{J}_1^p, \quad \vec{M}_1 = \vec{M}_1' + \vec{M}_1^p. \quad (4.8)$$

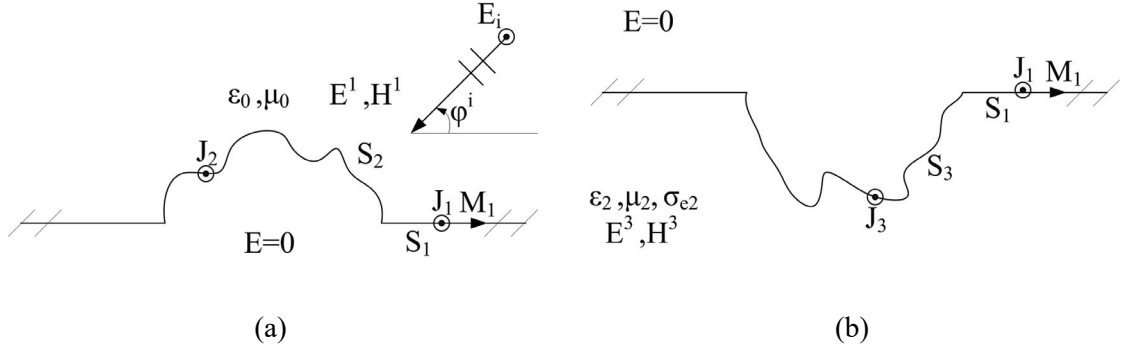


Figure 4.2 Application of the equivalence principle on the scatterer, (a) upper equivalence, (b) lower equivalence

The total E-field in region 1 for the upper equivalence is

$$\vec{E}^1 = \vec{E}^i + \vec{E}^{ref}(\vec{J}_1', \vec{M}_1') + \vec{E}^p(\vec{J}_1^p, \vec{M}_1^p) + \vec{E}^s(\vec{J}_2) + \vec{E}^{p2}(\vec{J}_v, \vec{M}_v). \quad (4.9)$$

Here, \vec{J}_2 is the equivalent electric current density on S_2 and \vec{J}_v and \vec{M}_v are the “vanished” electrical and magnetic current densities due to the presence of the scattering object as demonstrated on Figure 4.3.

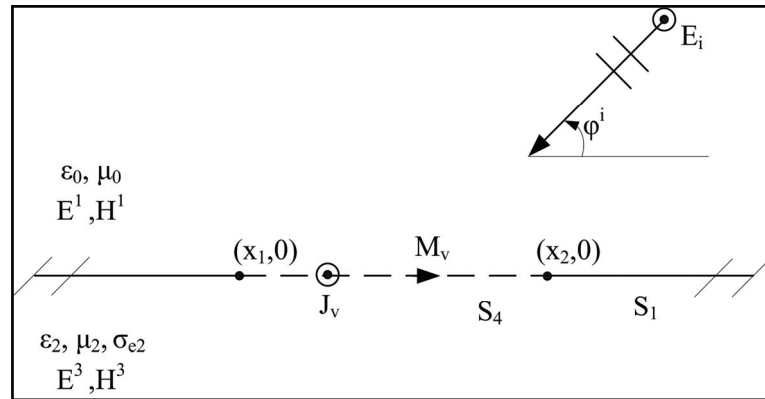


Figure 4.3 Demonstration of the vanished boundary plane region

where:

$$\vec{J}_v = -\vec{J}_1', \quad \vec{M}_v = -\vec{M}_1' \quad y=0, \quad x_1 < x < x_2 \quad (4.10)$$

Just outside region 1 $\vec{E}^i + \vec{E}^{ref}$ is zero on S_1 , using (4.9) total E-field on S_1 is written as:

$$\vec{E}^p(\vec{J}_1^p, \vec{M}_1^p) + \vec{E}^s(\vec{J}_2) = -\vec{E}^{p2}(\vec{J}_v, \vec{M}_v), \quad (4.11)$$

and on S_2 E-field satisfies:

$$\vec{E}^p(\vec{J}_1^p, \vec{M}_1^p) + \vec{E}^s(\vec{J}_2) = -\left[\vec{E}^i + \vec{E}^{ref}(\vec{J}', \vec{M}') + \vec{E}^{p2}(\vec{J}_v, \vec{M}_v) \right] = \vec{E}^{t2}. \quad (4.12)$$

On the other hand, the total E-field in region 2 for the lower equivalence is

$$\vec{E}^2 = \vec{E}^{trans}(\vec{J}', \vec{M}') + \vec{E}^p(-\vec{J}_1^p, -\vec{M}_1^p) + \vec{E}^s(\vec{J}_3) + \vec{E}^{p2}(\vec{J}_v, \vec{M}_v), \quad (4.13)$$

where \vec{J}_3 is the electrical current density on S_3 . Just outside region 2 \vec{E}^{trans} is zero on S_1 , using (4.13) total E-field on S_1 is written as:

$$\vec{E}^p(-\vec{J}_1^p, -\vec{M}_1^p) + \vec{E}^s(\vec{J}_3) = -\vec{E}^{p2}(\vec{J}_v, \vec{M}_v). \quad (4.14)$$

and on S_3 electrical field satisfies:

$$\vec{E}^p(-\vec{J}_1^p, -\vec{M}_1^p) + \vec{E}^s(\vec{J}_3) = -\left[\vec{E}^{trans}(\vec{J}', \vec{M}') + \vec{E}^{p2}(\vec{J}_v, \vec{M}_v) \right] = \vec{E}^{t2}, \quad (4.15)$$

where \vec{E}^{t2} is the known field on S_3 . After applying a MoM scheme based on pulse basis functions and point matching, the equations (4.11), (4.12), (4.14) and (4.15) become a set of linear equations, written in matrix form as

$$\begin{bmatrix} Z(k_0, \eta_0, S_1, S_1) & K(k_0, S_1, S_1) & Z(k_0, \eta_0, S_1, S_2) & [0] \\ Z(k_0, \eta_0, S_2, S_1) & K(k_0, S_2, S_1) & Z(k_0, \eta_0, S_2, S_2) & [0] \\ Z(k_2, \eta_2, S_1, S_1) & K(k_2, S_1, S_1) & [0] & Z(k_2, \eta_2, S_3, S_1) \\ Z(k_2, \eta_2, S_3, S_1) & K(k_2, S_3, S_1) & [0] & Z(k_2, \eta_2, S_3, S_3) \end{bmatrix} \begin{bmatrix} J_1^p \\ M_1^p \\ J_2 \\ J_3 \end{bmatrix} = \begin{bmatrix} E^{p2}(k_0, \eta_0, S_1) \\ E^{t2}(k_0, \eta_0, S_2) \\ E^{p2}(k_2, \eta_2, S_1) \\ E^{t2}(k_2, \eta_2, S_3) \end{bmatrix}, \quad (4.16)$$

where:

$$\begin{aligned} E^{p2}(k, \eta, S_m) &= \frac{k\eta}{4} \int_{x_1}^{x_2} J_v(x') H_0^{(2)}(k \|\vec{\rho}_m - x' \hat{x}\|) dx' \\ &+ \frac{jk}{4} \int_{x_1}^{x_2} M_v(x') H_1^{(2)}(k \|\vec{\rho}_m - x' \hat{x}\|) \frac{\hat{y} \cdot \vec{\rho}_m}{\|\vec{\rho}_m - x' \hat{x}\|} dx', \end{aligned} \quad (4.17)$$

and

$$E^{t2}(k, \eta, S_m) = \begin{cases} E^i + E^{ref} + E^{p2}(k, \eta, S_m) & y > 0 \\ E^{trans} + E^{p2}(k, \eta, S_m) & y < 0 \end{cases}. \quad (4.18)$$

Current densities, J_1^p , M_1^p , J_2 , and J_3 can be calculated by solving the matrix equation (4.16). Thereafter, the scattered electric field in region 1 can be calculated approximately using J_1^p , M_1^p , J_2 , J_v , and M_v with far field approximations:

$$\begin{aligned}
\vec{E}^s \cong & \frac{k_0 \eta_0}{4} \sqrt{\frac{2j}{\pi k_0 \rho}} e^{-jk_0 \rho} \left[\begin{array}{l} \sum_{i=1}^{N_1} \Delta_i (J_1^p)_i e^{jk_0 (x_i \cos \varphi + y_i \sin \varphi)} \\ + \sum_{l=1}^{N_2} \Delta_l (J_2)_l e^{jk_0 (x_l \cos \varphi + y_l \sin \varphi)} \end{array} \right] \hat{z} \\
& - \frac{k_0}{4} \sqrt{\frac{2j}{\pi k_0 \rho}} e^{-jk_0 \rho} \sum_{h=1}^{N_1} (-\cos \varphi \hat{y} + \sin \varphi \hat{x}) \cdot \hat{I}_h \Delta_h (M_1^p)_h e^{jk_0 (x_h \cos \varphi + y_h \sin \varphi)} \hat{z} \\
& + \frac{k_0}{2} \sqrt{\frac{2j}{\pi k_0 \rho}} e^{-jk_0 \rho} \left[(1 - \Gamma) \sin \varphi^i - (1 + \Gamma) \sin \varphi \right] \frac{e^{jk_0 x_1 (\cos \varphi + \cos \varphi^i)} - e^{jk_0 x_2 (\cos \varphi + \cos \varphi^i)}}{jk_0 (\cos \varphi + \cos \varphi^i)} \hat{z}.
\end{aligned} \tag{4.19}$$

The last term on (4.19) is derived from (4.17) using far field approximations, which is the field excited by J_v and M_v . Similarly, fields in region 2 can be calculated using J_1^p , M_1^p , J_3 , J_v and M_v .

4.3 Numerical Results

Firstly, monostatic scattering width of a perfectly conducting circular cylinder with radius equal to one wavelength half-buried in a material half space with different properties are calculated and compared with the series solution for scattering from a circular PEC bump on a PEC ground plane given on (2.8) is shown on Figure 4.4 with respect to incidence angle. As the reflection from the half space increases, results convergences to the series solution, as expected. In the calculation of red curve on Figure 4.4, electrical conductivity of the medium is chosen as almost infinite ($\sigma_e = 10^{10}$).

Secondly normalized electrical current induced on a PEC circular cylinder with a radius of quarter wavelength corresponding to medium of region 2, half-buried in a material half space with $\epsilon_r = 4$, $\mu_r = 1$ and $\sigma_e = 0$ is investigated and presented with the results of [2] on Figure 4.5 for different incidence angles. As can be seen on this figure, both results agree very well.

Thirdly, normalized current density on a half-buried rectangular cylinder with a height of 1.25λ and a width of 0.625λ for an illumination angle of $\varphi^i = 155^\circ$ with respect to polar position is presented on Figure 4.6 compared with free space MoM result (Red curve) and different electrical properties of the medium filling the half space. According to the results, current density distribution is continuous, except the angles corresponding to edges, which are known to be of singular behavior for this configuration. In addition

to this, exponential decay of current density can be observed comparing blue and green curves for polar angles greater than 180° .

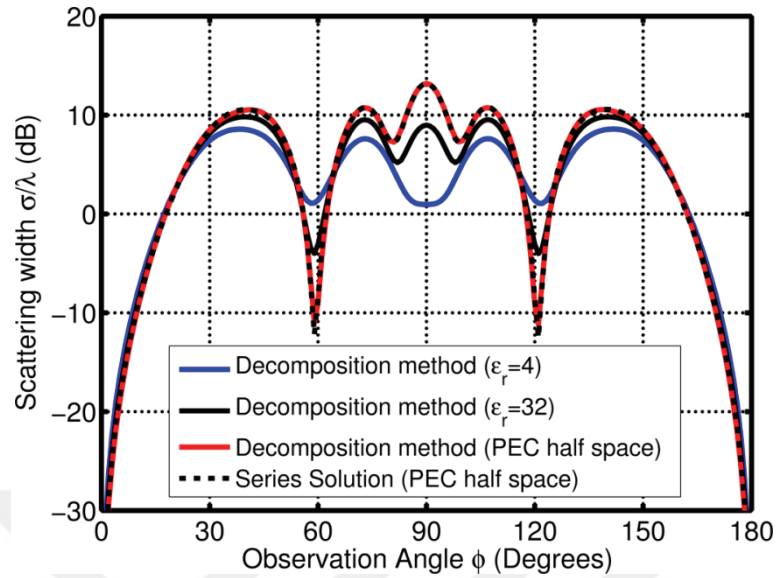


Figure 4.4 Scattering width of a half-buried circular cylinder with radius λ

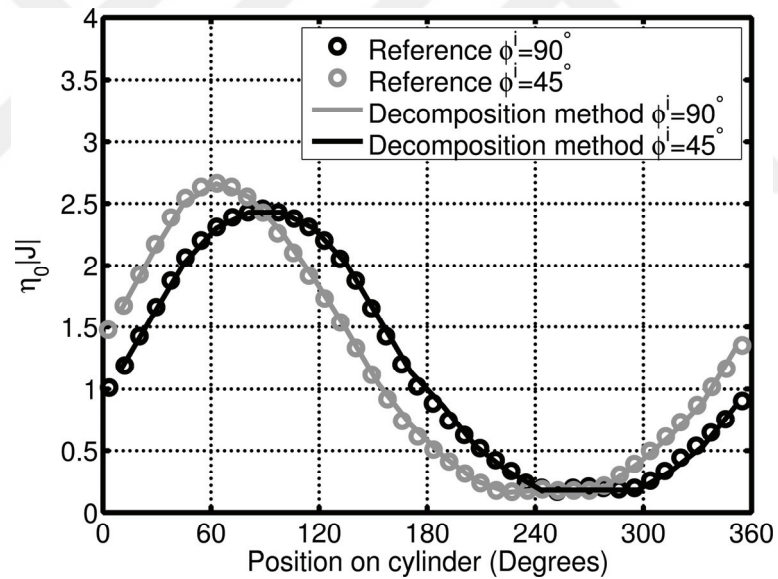


Figure 4.5 Current induced on a PEC circular cylinder half-buried in a material with $\epsilon_r = 4$, $\mu_r = 1$ and $\sigma_e = 0$ for different incidence angles

Normalized perturbed electric and magnetic current densities for green curve on Figure 4.6 are presented on Figure 4.7 as example.

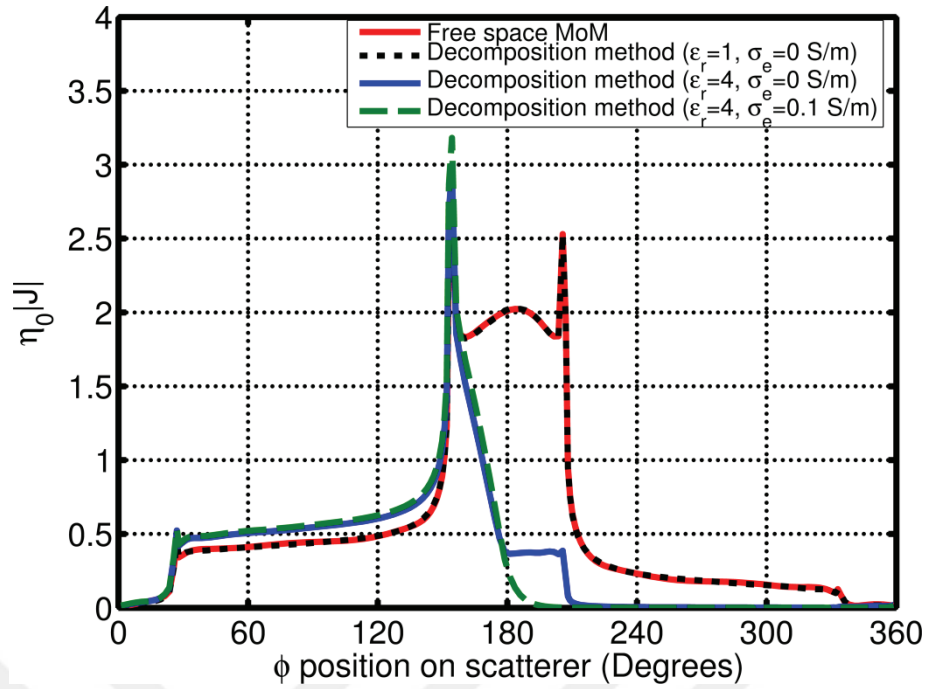


Figure 4.6 Current induced on a half-buried PEC rectangular cylinder for different medium parameters

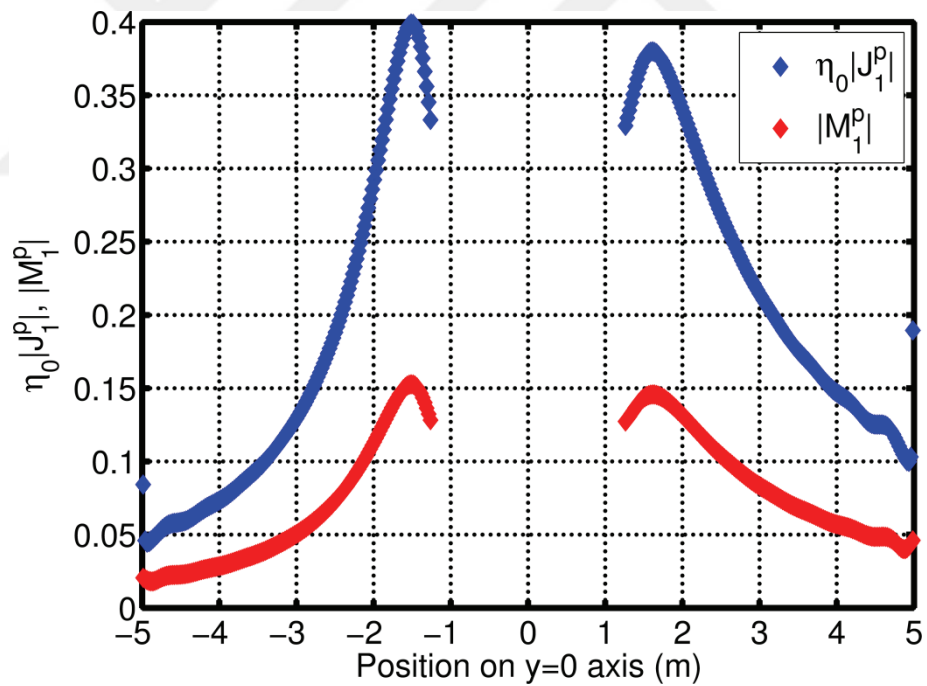


Figure 4.7 Perturbated current densities for green curve on Figure 4.6

Lastly, a range profile calculation is performed for a half-buried square cylinder with a height b and width a of one meter, for an incidence and observation angle of $\varphi = \varphi^i = 100^\circ$ for different medium parameters are presented on Figure 4.8. Calculation

is performed using inverse discrete Fourier transform, at a center frequency of 25 GHz and using a bandwidth of 3.71 GHz .

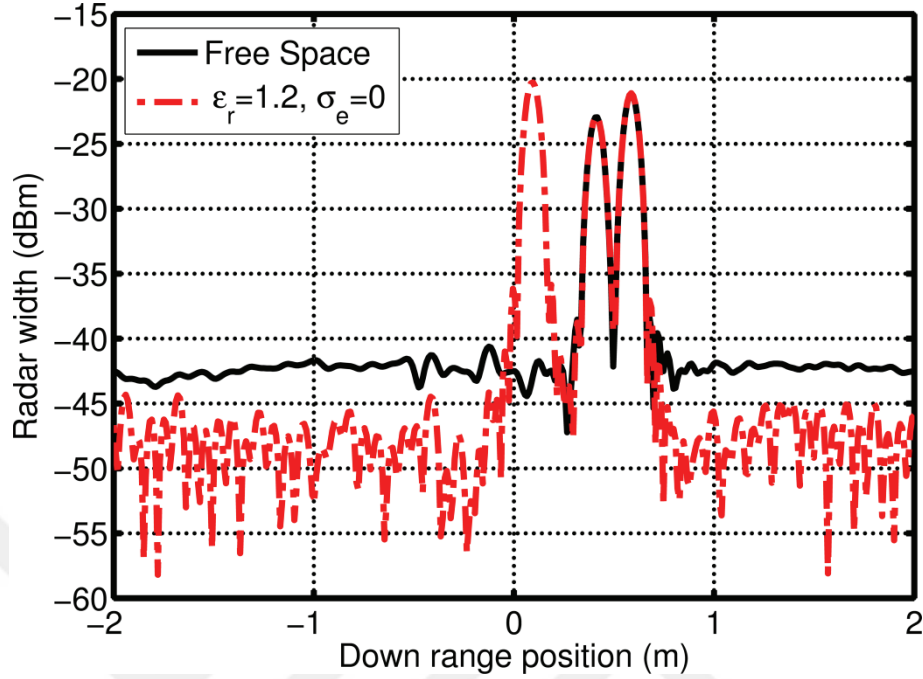


Figure 4.8 Range profiles for the half-buried square cylinder

In order to investigate this result, one can refer to Figure 4.9, which demonstrates discontinuity positions of the scattering problem with respect to the reference phase plane. From the geometry, distances L_{1-6} can be calculated as:

$$L_1 = L_4 = \frac{\sqrt{a^2 + b^2}}{2} \sin[\alpha + (\varphi^i - 90)], \quad (4.20)$$

$$L_2 = L_3 = \frac{\sqrt{a^2 + b^2}}{2} \sin[\alpha - (\varphi^i - 90)], \quad (4.21)$$

$$L_5 = L_6 = \frac{a}{2} \sin(\varphi^i - 90). \quad (4.22)$$

Here $\alpha = \arctan(b/a)$. According to Figure 4.8, two dominant scattering centers for free space and three for $\epsilon_r = 1.2$ can be observed. Inspecting the range profiles, peaks at positions 0.58, 0.41, and 0.09m are thought to correspond to $L_1 = 0.5792$, $L_2 = 0.4056$ and $L_5 = 0.0868$ m. Third scattering center at 0.09m is due to interaction of the scatterer and the material half space. Other discontinuities are not dominant because of the high calculation frequency.

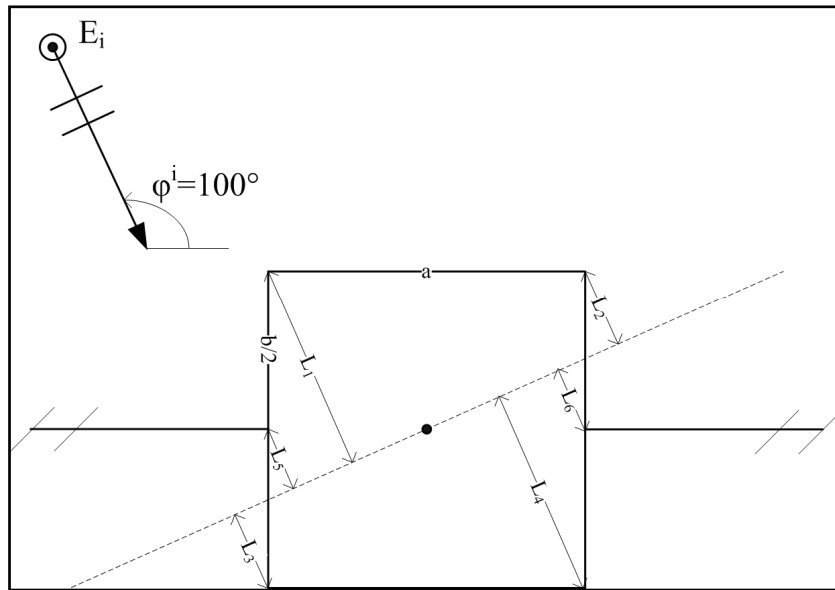


Figure 4.9 Geometry for analyzing the range profile

SCATTERING FROM A CYLINDER PARTIALLY BURIED IN
A DIELECTRIC HALF SPACE WITH AN ARBITRARY
PERIODIC BOUNDARY PLANE PROFILE

5.1 Introduction

In this chapter, scattering from a two-dimensional object, with a dielectric permittivity of ϵ_1 , magnetic permeability of μ_1 and electrical conductivity of σ_{e1} which is partially buried in a dielectric half-space which has a dielectric permittivity of ϵ_2 , magnetic permeability of μ_2 and electrical conductivity of σ_{e2} , with an arbitrary periodic boundary plane profile with a period of L is investigated by a decomposition method. The object with arbitrary cross section is defined by surfaces S_2 and S_3 , depicted on Figure 5.1, where S_2 is in the upper half-space ($y > 0$) and S_3 is in the lower half-space ($y < 0$).

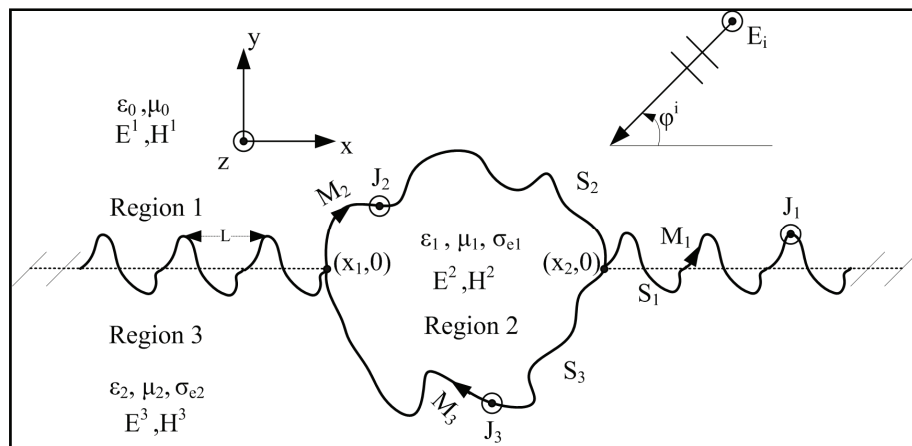


Figure 5.1 Scattering geometry

A TM_z polarized plane wave with electric field component given on (2.1) is incident on the object with the incidence angle φ^i .

5.2 Scattering from a Dielectric Half Space with a Periodic Boundary Surface

In order to solve the scattering problem, firstly plane wave scattering from the periodic structure is considered. This problem is solved with MoM with surface equivalency method. A TM_z polarized plane wave defined on (2.1) is incident on the dielectric half space with periodic boundary surface, which has a period of, L and an arbitrary profile S_p depicted on Figure 5.2. Half space has a dielectric permittivity of ϵ_2 , magnetic permeability of μ_2 and electrical conductivity of σ_{e2} .

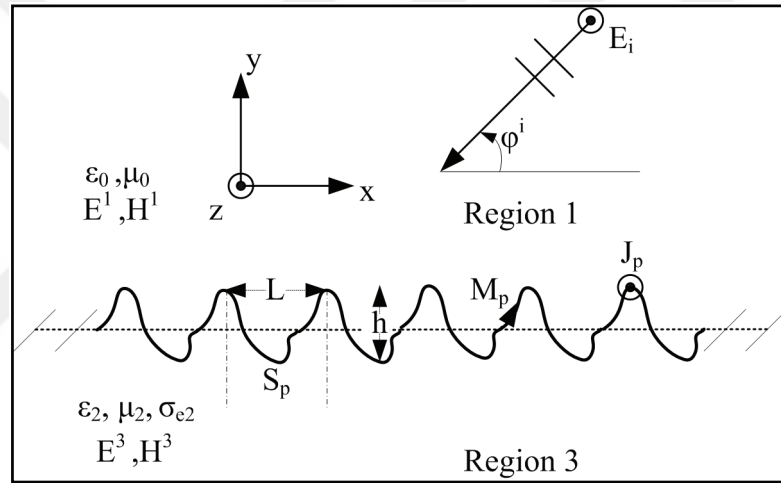


Figure 5.2 Periodic boundary interface surface

Plane wave induces equivalent electric and magnetic surface current densities \vec{J}_p and \vec{M}_p . Total E-field in region 1 is the summation of the incident field and the scattered field due to the current densities. However, in region 2 only the scattered field exists. Periodic Green's function for this problem is [25]:

$$G_{1,3}(\vec{\rho} | \vec{\rho}') = -\frac{j}{2L} \sum_{n=-\infty}^{\infty} \frac{e^{-j\beta_n^{1,3}(x-x')} e^{-jq_n^{1,3}|y-y'|}}{q_n^{1,3}} \quad (5.1)$$

where:

$$q_n^{1,3} = -j\sqrt{\beta_n^{1,3} - k_{1,3}^2} \quad (5.2)$$

$$\beta_n^{1,3} = \beta^{1,3} + \frac{2n\pi}{L} \quad (5.3)$$

and

$$\beta^{1,3} = k_{1,3} \cos \varphi_i \quad (5.4)$$

where indices 1 and 3 indicates regions 1 and 3. Integral equation for magnetic and electric vector potentials:

$$\vec{A}^{1,3} = \mu_{1,3} \int_{S_p} \vec{J}_p(\vec{\rho}') G_{1,3}(\vec{\rho} | \vec{\rho}') dl' \quad (5.5)$$

$$\vec{F}^{1,3} = \varepsilon_{1,3} \int_{S_p} \vec{M}_p(\vec{\rho}') G_{1,3}(\vec{\rho} | \vec{\rho}') dl' \quad (5.6)$$

electric field using this potentials:

$$\vec{E}^{1,3} = -j\omega \vec{A}^{1,3} - \frac{1}{\varepsilon_{1,3}} \nabla \times \vec{F}^{1,3} \quad (5.7)$$

yields:

$$\begin{aligned} \vec{E}^{1,3} = & -j\omega \mu_{1,3} \int_{S_p} \vec{J}_p(\vec{\rho}') G_{1,3}(\vec{\rho} | \vec{\rho}') dl' \\ & - \frac{1}{2L} \int_{S_p} \vec{M}_p(\vec{\rho}') \times \sum_{n=-\infty}^{\infty} \frac{e^{-j\beta_n^{1,3}(x-x')} e^{-jq_n^{1,3}|y-y'|}}{q_n^{1,3}} \left[\beta_n^{1,3} \hat{x} + \text{sign}(y-y') q_n^{1,3} \hat{y} \right] dl'. \end{aligned} \quad (5.8)$$

Using equivalency principle, taking fields in region 3 as zero, just outside region 1 on S_p total E-field satisfies

$$\vec{E}^i + \vec{E}_1 = 0 \quad (5.9)$$

and taking fields in region 1 as zero, just outside region 3 on S_p scattered field satisfies

$$\vec{E}_3 = 0. \quad (5.10)$$

Applying a MoM scheme with pulse basis functions and Dirac test functions (5.9) and (5.10) can be written in matrix form as:

$$\begin{bmatrix} A_1 & B_1 \\ A_3 & B_3 \end{bmatrix} \begin{bmatrix} J_p \\ M_p \end{bmatrix} = \begin{bmatrix} C \\ [0] \end{bmatrix} \quad (5.11)$$

where

$$(A_{1,3})_{i,l} = -\frac{k_{1,3} \eta_{1,3}}{2L} \frac{j}{I_{iy}} \sum_{n=-\infty}^{\infty} \frac{e^{-j\beta_n^{1,3}(x_l-x_i)} g_{i,l}^{1,3}}{q_n^{1,3}}, \quad (5.12)$$

$$g_{i,l}^{1,3} = \begin{cases} \left[e^{j\zeta_i^{1,3}|I_{iy}|\frac{\Delta_i}{2}} - e^{-j\zeta_i^{1,3}|I_{iy}|\frac{\Delta_i}{2}} \right] \frac{e^{-jq_n^{1,3}(y_l-y_i)}}{\zeta_i^{1,3}} & y_l > y_i \\ \left[e^{j\zeta_i^{1,3}|I_{iy}|\frac{\Delta_i}{2}} - e^{-j\zeta_i^{1,3}|I_{iy}|\frac{\Delta_i}{2}} \right] \frac{e^{jq_n^{1,3}(y_l-y_i)}}{\zeta_i^{1,3}} & y_l < y_i, \\ \frac{1 - e^{-j\zeta_i^{1,3}\frac{\Delta_i}{2}}}{\zeta_i^{1,3}} + \frac{e^{j\psi_i^{1,3}\frac{\Delta_i}{2}} - 1}{\psi_i^{1,3}} & y_l = y_i \end{cases} \quad (5.13)$$

$$\zeta_i^{1,3} = \begin{cases} \xi_i^{1,3} & y_l > y_i \\ \psi_i^{1,3} & y_l < y_i \end{cases}, \quad (5.14)$$

$$\xi_i^{1,3} = \beta_n^{1,3} I_{ix} + q_n^{1,3} |I_{iy}|, \quad (5.15)$$

$$\psi_i^{1,3} = \beta_n^{1,3} I_{ix} - q_n^{1,3} |I_{iy}|, \quad (5.16)$$

$$(B_{1,3})_{i,l} = \frac{1}{2L} \sum_{n=-\infty}^{\infty} e^{-j\beta_n^{1,3}(x_l-x_i)} h_{i,l}^{1,3}, \quad (5.17)$$

$$h_{i,l}^{1,3} = \begin{cases} -\left(\frac{\beta_n^{1,3}}{q_n^{1,3}} I_{iy} - I_{ix} \right) e^{-jq_n^{1,3}(y_l-y_i)} \frac{e^{j\zeta_i^{1,3}\frac{\Delta_i}{2}} - e^{-j\zeta_i^{1,3}\frac{\Delta_i}{2}}}{j\zeta_i^{1,3}} & y_l > y_i \\ -\left(\frac{\beta_n^{1,3}}{q_n^{1,3}} I_{iy} + I_{ix} \right) e^{jq_n^{1,3}(y_l-y_i)} \frac{e^{j\zeta_i^{1,3}\frac{\Delta_i}{2}} - e^{-j\zeta_i^{1,3}\frac{\Delta_i}{2}}}{j\zeta_i^{1,3}} & y_l < y_i \\ \left(-\frac{\beta_n^{1,3}}{q_n^{1,3}} I_{iy} + I_{ix} \right) \frac{1 - e^{-j\zeta_i^{1,3}\frac{\Delta_i}{2}}}{j\zeta_i^{1,3}} + \left(\frac{\beta_n^{1,3}}{q_n^{1,3}} I_{iy} + I_{ix} \right) \frac{e^{j\psi_i^{1,3}\frac{\Delta_i}{2}} - 1}{j\psi_i^{1,3}} & y_l = y_i, I_{iy} > 0 \\ -\left(\frac{\beta_n^{1,3}}{q_n^{1,3}} I_{iy} + I_{ix} \right) \frac{1 - e^{-j\psi_i^{1,3}\frac{\Delta_i}{2}}}{j\psi_i^{1,3}} + \left(-\frac{\beta_n^{1,3}}{q_n^{1,3}} I_{iy} + I_{ix} \right) \frac{e^{j\zeta_i^{1,3}\frac{\Delta_i}{2}} - 1}{j\zeta_i^{1,3}} & y_l = y_i, I_{iy} < 0 \end{cases} \quad (5.18)$$

and

$$(C)_l = e^{jk_0(x_l \cos \varphi_l + y_l \sin \varphi_l)}. \quad (5.19)$$

Here i and l indicates source and observation segment index, I_{ix} and I_{iy} are the x and y component of the tangent unit vector of the source segment index, Δ_i is the length of the source segment and $x_{i,l}$ and $y_{i,l}$ are the x and y component of the source and observation segment respectively.

Current densities J_p and M_p are calculated by solving (5.11). At this point it should be noted that J_p and M_p are the current densities corresponding to the first period. For other periods these current densities should be corrected by

$$\mathbf{J}'_p = e^{-jm\beta L} \mathbf{J}_p, \mathbf{M}'_p = e^{-jm\beta L} \mathbf{M}_p, \quad (5.20)$$

where m is the period index of the infinite surface. Scattered E-field can be calculated using these current densities using (5.8) with (5.12) and (5.17) as.

$$\vec{E}_{1,3} = \sum_{i=1}^N (\mathbf{J}_p)_i (A_{1,3})_i \hat{z} + \sum_{i=1}^N (\mathbf{M}_p)_i (B_{1,3})_i \hat{z} \quad (5.21)$$

where x_i and y_i indicates the observation point which the scattered E-field will be calculated and N is the number of linear segments in a period used in the calculation.

5.3 Solution by the Decomposition Method

When the scattering body is not present, for region 1, there will be incident and field scattered from the half space. However, for region 3 there will only be the field scattered from the half space:

$$\vec{E}^{Total} = \begin{cases} \vec{E}^i + \vec{E}_1(\vec{J}_p, \vec{M}_p) & \text{region 1} \\ \vec{E}_3(\vec{J}_p, \vec{M}_p) & \text{region 3} \end{cases}. \quad (5.22)$$

In the presence of the object, using surface equivalence principle, the problem can be decomposed into three parts, which are the upper equivalency for region 1, internal equivalency for region 2 and the lower equivalency for the region 3 as shown in Figure 5.3. At this point, electrical and magnetic current densities \vec{J}_1^p and \vec{M}_1^p are introduced on the surface S_1 , near the object. Therefore, the total current densities \vec{J}_1 and \vec{M}_1 on S_1 are:

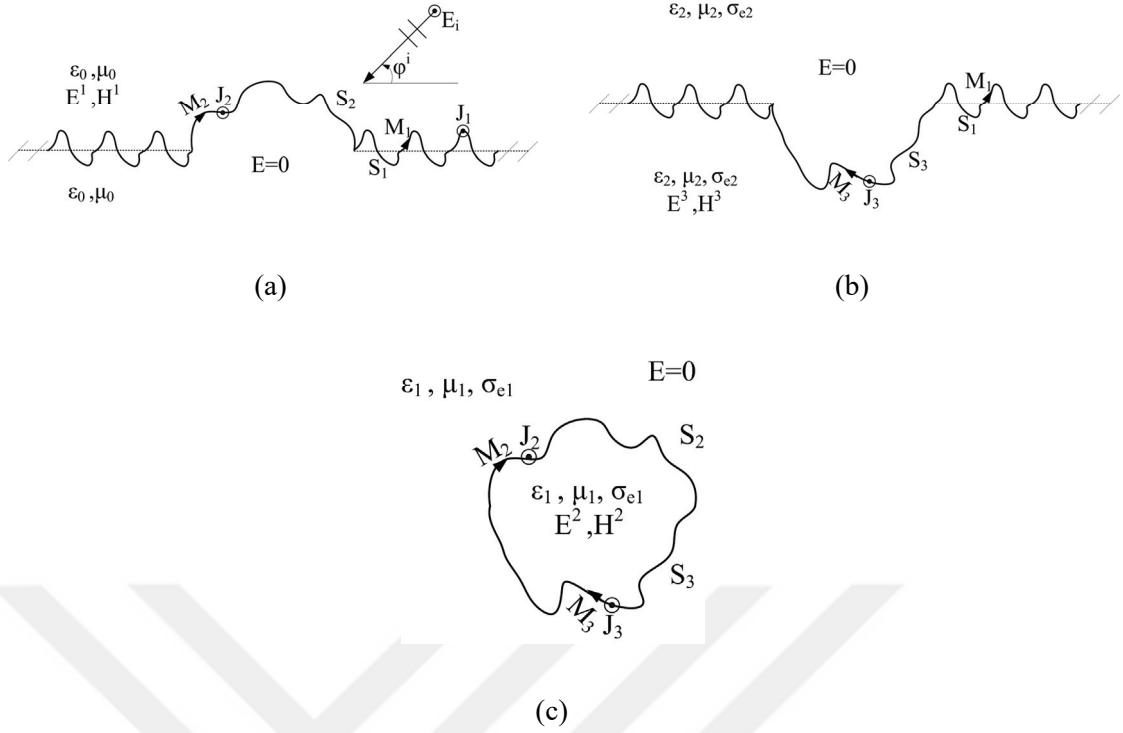


Figure 5.3 Application of the equivalency principle on the scatterer, (a) upper equivalence, (b) lower equivalence and (c) internal equivalence

$$\vec{J}_1 = \vec{J}_p' + \vec{J}_1^p, \quad \vec{M}_1 = \vec{M}_p' + \vec{M}_1^p. \quad (5.23)$$

The total E-field in region 1 for the upper equivalence is

$$\vec{E}^{T1} = \vec{E}^i + \vec{E}^1(\vec{J}_p, \vec{M}_p) + \vec{E}^p(\vec{J}_1^p, \vec{M}_1^p) + \vec{E}^s(\vec{J}_2, \vec{M}_2) + \vec{E}^{p3}(\vec{J}_v, \vec{M}_v). \quad (5.24)$$

Here \vec{M}_2 is the magnetic current density on S_2 and \vec{J}_v and \vec{M}_v are the “vanished” electrical and magnetic current densities due to the presence of the scattering object, which are the negative of the current densities \vec{J}_p' and \vec{M}_p' :

$$\vec{J}_v = -\vec{J}_p', \quad \vec{M}_v = -\vec{M}_p' \quad x_1 < x < x_2. \quad (5.25)$$

Just outside region 1 $\vec{E}^i + \vec{E}^1$ is zero on S_1 , using (5.24) total E-field on S_1 is written as:

$$\vec{E}^p(\vec{J}_1^p, \vec{M}_1^p) + \vec{E}^s(\vec{J}_2, \vec{M}_2) = -\vec{E}^{p3}(\vec{J}_v, \vec{M}_v), \quad (5.26)$$

and on S_2 E-field satisfies:

$$\vec{E}^p(\vec{J}_1^p, \vec{M}_1^p) + \vec{E}^s(\vec{J}_2, \vec{M}_2) = -[\vec{E}^i + \vec{E}^1(\vec{J}_p, \vec{M}_p) + \vec{E}^{p3}(\vec{J}_v, \vec{M}_v)] = \vec{E}^{t3}. \quad (5.27)$$

On the other hand, the total E-field in region 2 just outside region 2 on S_2 and S_3 E-field satisfies

$$\vec{E}^s(-\vec{J}_2, -\vec{M}_2) + \vec{E}^s(-\vec{J}_3, -\vec{M}_3) = 0, \quad (5.28)$$

where \vec{M}_3 is the magnetic current density on S_3 . Total E-field in region 3 for the lower equivalence is

$$\vec{E}^{T3} = \vec{E}^3(\vec{J}_p, \vec{M}_p) + \vec{E}^p(-\vec{J}_1^p, -\vec{M}_1^p) + \vec{E}^s(\vec{J}_3, \vec{M}_3) + \vec{E}^{p3}(\vec{J}_v, \vec{M}_v). \quad (5.29)$$

Just outside region 3 \vec{E}^3 is zero on S_1 , using (5.28) total E-field on S_1 is written as:

$$\vec{E}^p(-\vec{J}_1^p, -\vec{M}_1^p) + \vec{E}^s(\vec{J}_3, \vec{M}_3) = -\vec{E}^{p3}(\vec{J}_v, \vec{M}_v). \quad (5.30)$$

and on S_3 electrical field satisfies:

$$\vec{E}^p(-\vec{J}_1^p, -\vec{M}_1^p) + \vec{E}^s(\vec{J}_3, \vec{M}_3) = -\left[\vec{E}^3(\vec{J}_p, \vec{M}_p) + \vec{E}^{p3}(\vec{J}_v, \vec{M}_v) \right] = \vec{E}^{t3}, \quad (5.31)$$

After applying a MoM scheme based on pulse basis functions and point matching, the equations (5.26), (5.27), (5.28), (5.30) and (5.31) become a set of linear equations, written in matrix form as

$$\begin{bmatrix} Z(k_0, \eta_0, S_1, S_1) & K(k_0, S_1, S_1) & Z(k_0, \eta_0, S_1, S_2) & K(k_0, S_1, S_2) & [0] & [0] \\ Z(k_0, \eta_0, S_2, S_1) & K(k_0, S_2, S_1) & Z(k_0, \eta_0, S_2, S_2) & K(k_0, S_2, S_2) & [0] & [0] \\ [0] & [0] & Z(k_1, \eta_1, S_2, S_2) & K(k_1, S_2, S_2) & Z(k_1, \eta_1, S_2, S_3) & K(k_1, S_2, S_3) \\ [0] & [0] & Z(k_1, \eta_1, S_3, S_2) & K(k_1, S_3, S_2) & Z(k_1, \eta_1, S_3, S_3) & K(k_1, S_3, S_3) \\ Z(k_2, \eta_2, S_1, S_1) & K(k_2, S_1, S_1) & [0] & [0] & Z(k_2, \eta_2, S_1, S_3) & K(k_2, S_1, S_3) \\ Z(k_2, \eta_2, S_3, S_1) & K(k_2, S_3, S_1) & [0] & [0] & Z(k_2, \eta_2, S_3, S_3) & K(k_2, S_3, S_3) \end{bmatrix} \begin{bmatrix} J_1^p \\ M_1^p \\ J_2 \\ M_2 \\ J_3 \\ M_3 \end{bmatrix} = \begin{bmatrix} E^{p3}(k_0, \eta_0, S_1) \\ E^{t3}(k_0, \eta_0, S_2) \\ [0] \\ [0] \\ E^{p3}(k_2, \eta_2, S_1) \\ E^{t3}(k_2, \eta_2, S_3) \end{bmatrix}, \quad (5.32)$$

where:

$$\begin{aligned} E^{p3}(k, \eta, S_m) &= \frac{k\eta}{4} \sum_{i=1}^{N_v} (J_v)_i \int_{-\Delta_i/2}^{\Delta_i/2} H_0^{(2)}(k \|\vec{\rho}_m - \vec{\rho}_i - l' \hat{I}_i\|) dl' \\ &+ \frac{jk}{4} \sum_{i=1}^{N_v} (M_v)_i \int_{-\Delta_i/2}^{\Delta_i/2} H_1^{(2)}(k \|\vec{\rho}_m - \vec{\rho}_i - l' \hat{I}_i\|) \frac{\hat{n}_i \cdot (\vec{\rho}_m - \vec{\rho}_i)}{\|\vec{\rho}_m - \vec{\rho}_i - l' \hat{I}_i\|} dl', \end{aligned} \quad (5.33)$$

and:

$$E^{t3}(k, \eta, S_m) = \begin{cases} E^i + \vec{E}^1(\vec{J}_p, \vec{M}_p) + E^{p3}(k, \eta, S_m) & y > 0 \\ \vec{E}^3(\vec{J}_p, \vec{M}_p) + E^{p3}(k, \eta, S_m) & y < 0 \end{cases}, \quad (5.34)$$

where N_v is the number of segments within the region $x_2 > x > x_1$ on S_1 , $\vec{\rho}_i$ is the center of the i^{th} segment, \hat{n}_i is the normal vector of the i^{th} segment, \hat{I}_i is the tangent

vector of the i^{th} segment and $\bar{\rho}_m$ is the center of the m^{th} observation segment. Current densities J_1^p , M_1^p , J_2 , M_2 , J_3 , and M_3 are can be calculated by solving the matrix equation (5.32). Thereafter, the scattered electric field in region 1 is calculated approximately using J_1^p , M_1^p , J_2 , M_2 , J_v , and M_v with far field approximations:

$$\begin{aligned}
\bar{E}^s \cong & \frac{k_0 \eta_0}{4} \sqrt{\frac{2j}{\pi k_0 \rho}} e^{-jk_0 \rho} \left[\sum_{i=1}^{N_1} \Delta_i (J_1^p)_i e^{jk_0(x_i \cos \varphi + y_i \sin \varphi)} \right. \\
& \left. + \sum_{l=1}^{N_2} \Delta_l (J_2)_l e^{jk_0(x_l \cos \varphi + y_l \sin \varphi)} \right] \hat{z} \\
& - \frac{k_0}{4} \sqrt{\frac{2j}{\pi k_0 \rho}} e^{-jk_0 \rho} \left[\sum_{i=1}^{N_1} (-\cos \varphi \hat{y} + \sin \varphi \hat{x}) \cdot \hat{I}_i \Delta_i (M_1^p)_i e^{jk_0(x_i \cos \varphi + y_i \sin \varphi)} \right. \\
& \left. + \sum_{l=1}^{N_2} (-\cos \varphi \hat{y} + \sin \varphi \hat{x}) \cdot \hat{I}_l \Delta_l (M_2)_l e^{jk_0(x_l \cos \varphi + y_l \sin \varphi)} \right] \hat{z} \\
& + \frac{k_0 \eta_0}{4} \sqrt{\frac{2j}{\pi k_0 \rho}} e^{-jk_0 \rho} \left[\sum_{i=1}^{N_v} \Delta_i (J_v)_i e^{jk_0(x_i \cos \varphi + y_i \sin \varphi)} \right] \hat{z} \\
& - \frac{k_0}{4} \sqrt{\frac{2j}{\pi k_0 \rho}} e^{-jk_0 \rho} \left[\sum_{i=1}^{N_v} (-\cos \varphi \hat{y} + \sin \varphi \hat{x}) \cdot \hat{I}_i \Delta_i (M_v)_i e^{jk_0(x_i \cos \varphi + y_i \sin \varphi)} \right] \hat{z}.
\end{aligned} \tag{5.35}$$

Similarly, fields in region 3 can be calculated using J_1^p , M_1^p , J_3 , M_3 , J_v , and M_v and the fields in region 2 can be calculated using J_2 , M_2 , J_3 , and M_3 .

5.4 Numerical Results

In order to verify validity of the method, several examples are presented in this section. Firstly, electrical current density distribution on an infinite perfectly conducting surface with a sinusoidal surface height profile is considered. Plane wave is incident on the surface with an angle of $\varphi^i = 165^\circ$, surface profile has a peak height of 0.25λ and a period of 3.9λ . Real and imaginary parts of the current density calculated using the procedure described in section 5.2 are presented on Figure 5.4 compared with the reference solution given on [26]. As can be seen from the figure results agree very well.

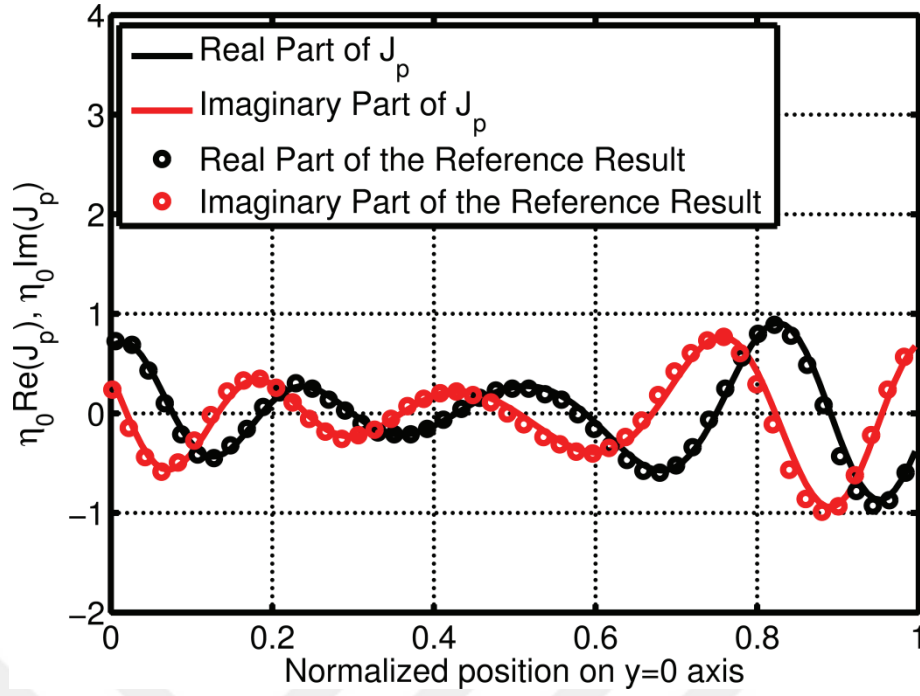


Figure 5.4 Current density distribution on the periodic surface for one period

Afterwards, equivalent electrical and magnetic current densities calculated by choosing medium of the region 3 as free space. Peak amplitude of the surface height profile is chosen to be almost zero ($10^{-10} \lambda$), the period length is chosen as λ and the incidence angle is chosen as $\varphi^i = 45^\circ$. Calculated values are compared with the current densities calculated with expressions (4.4) and (4.5) and presented on Figure 5.5 and Figure 5.6 for electrical and magnetic current densities respectively. Results are consistent with the reference results.

Next, monostatic scattering from a conducting circular cylinder with radius λ on an infinite electrically conducting ground plane, which corresponds to semicircular bump on a perfectly conducting infinite ground plane, which is considered on previous Chapters. Scattering width versus observation angle is presented on Figure 5.7 for various sinusoidal periodic surface peak amplitudes and for a period of 5λ compared with the series solution given by (2.8) and calculation result for a flat surface interface. As can be seen from Figure 5.7, scattering width calculated by the series solution, for flat surface and result of $h = 10^{-10}$ m are almost identical. On the other hand, as the value of h increases, calculation results starts to diverge from the series solution result, as expected.

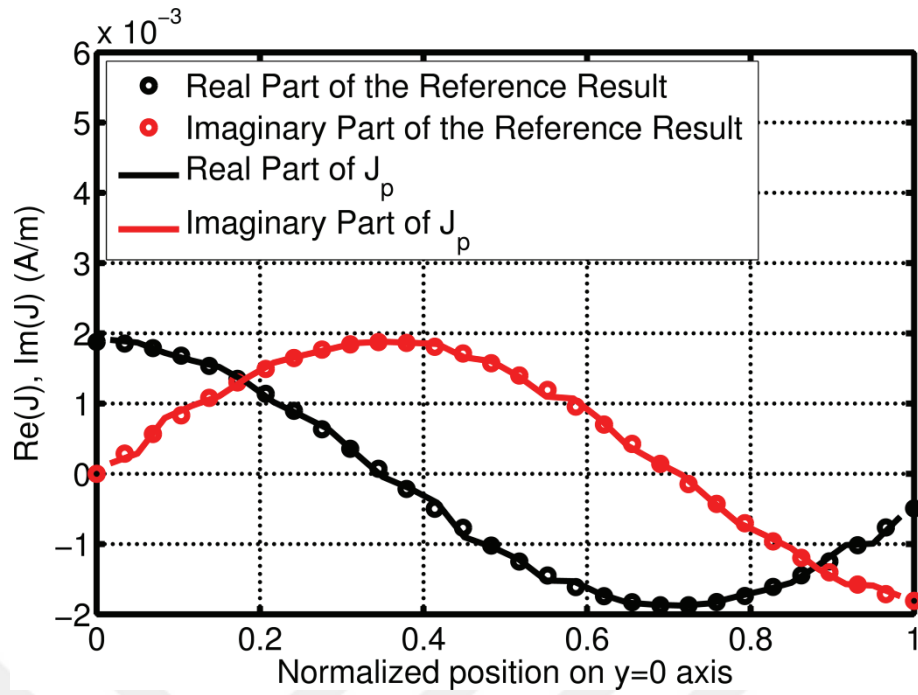


Figure 5.5 Electrical current density distribution on the periodic surface for one period

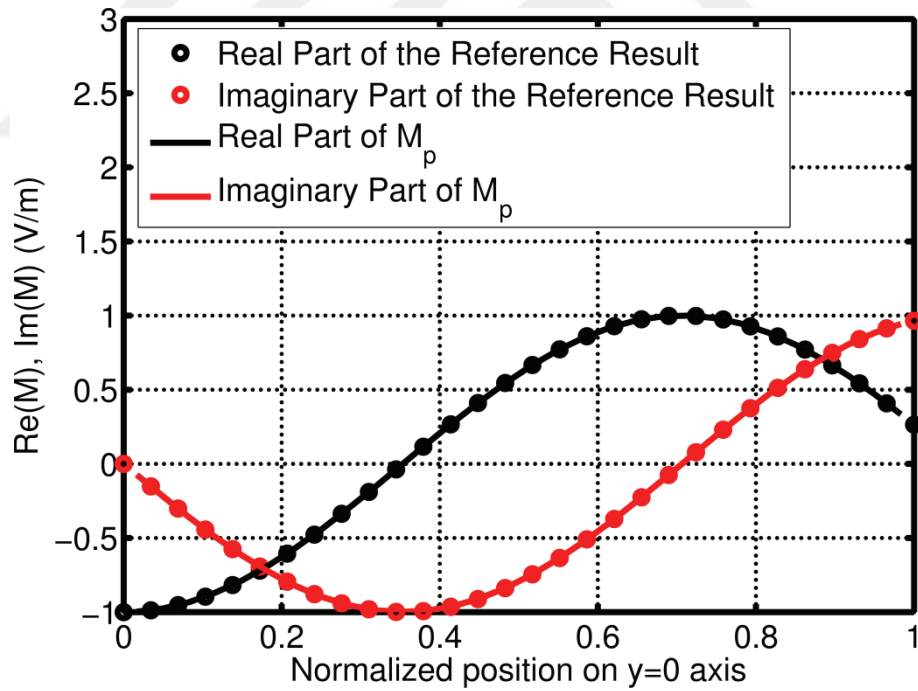


Figure 5.6 Magnetic current density distribution on the periodic surface for one period

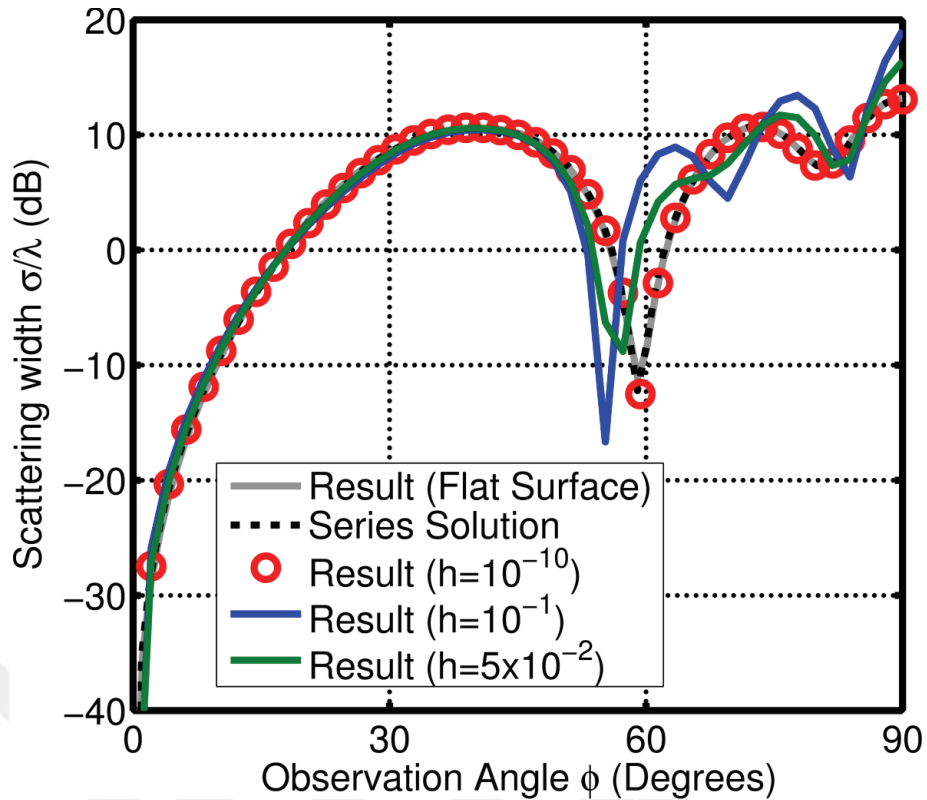


Figure 5.7 Scattering width of a semicircular bump with radius λ on an infinite perfectly conducting ground plane with periodic sinusoidal interface surface height profile

Then, in order to investigate error caused by the approximations of the decomposition method, monostatic scattering width of a circular cylinder with a radius of λ with electrical parameters of free space, semi-buried in a material half space with electrical parameters of free space shown on Figure 5.8 is calculated and given on Figure 5.9. As can be seen from the figure, for this case, error level associated with the approximations is under 10^{-3} in terms of scattering width.

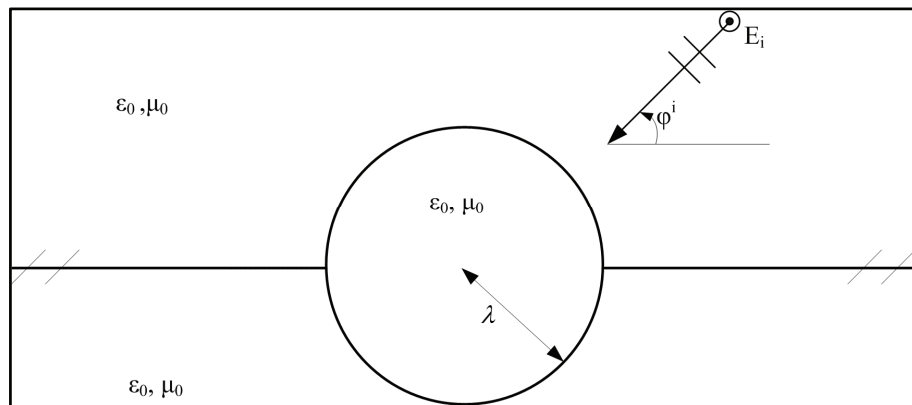


Figure 5.8 Geometry of a circular cylinder with material properties of free space, semi-buried in a half space with free space parameters

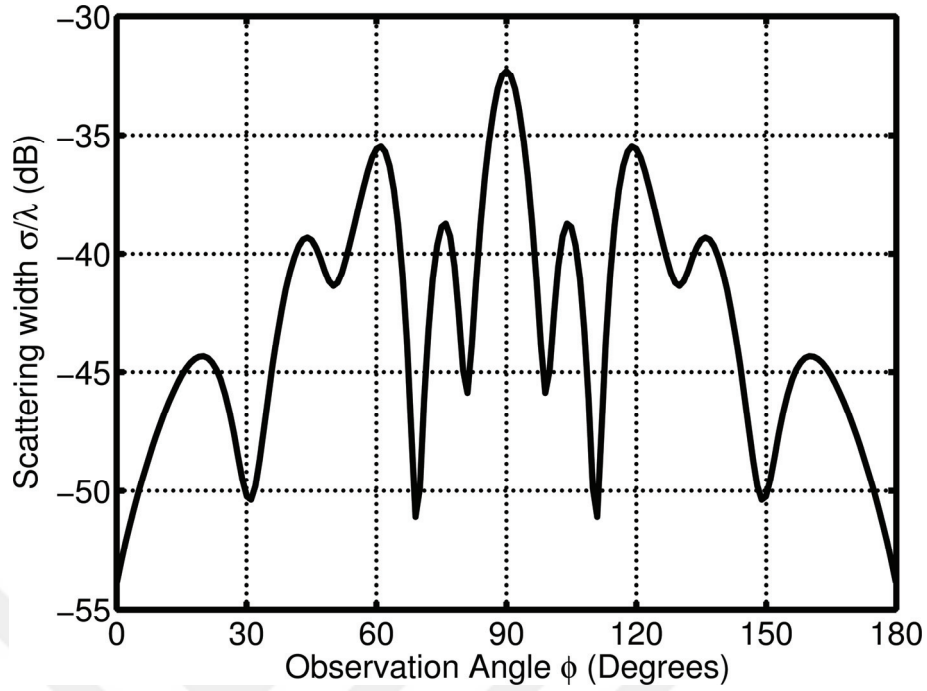


Figure 5.9 Scattering width of a circular cylinder with electrical properties of free space, semi-buried in a half space with electrical properties of free space

Then, current density induced on a highly conducting ($\sigma_{e1} = 10^{10}$) cylinder with a radius of λ semi-buried in a material half space with free space electrical parameters is calculated and presented on Figure 5.10 compared with MoM result for a PEC cylinder in free space. Plane wave is incident on the scatterer with an angle of $\varphi^i = 90^\circ$. As can be seen from the figure results agree very well.

Afterwards, monostatic scattering from a cylinder with elliptical cross section half buried in a highly electrically conducting ($\sigma_{e2} = 10^{10}$) half space with a periodic sinusoidal interface profile is examined, which is investigated previously on Chapter 3 (Figure 3.8). Sinusoidal surface profile has a peak amplitude of 10^{-10} m and has a period of 5 m. The cylinder has a relative dielectric permittivity of $\epsilon_{r1} = 3$, relative magnetic permeability of $\mu_{r1} = 1$ and electrical conductivity of $\sigma_{e1} = 0$. Calculation results are shown on Figure 5.11 compared with the series solution result of [16].

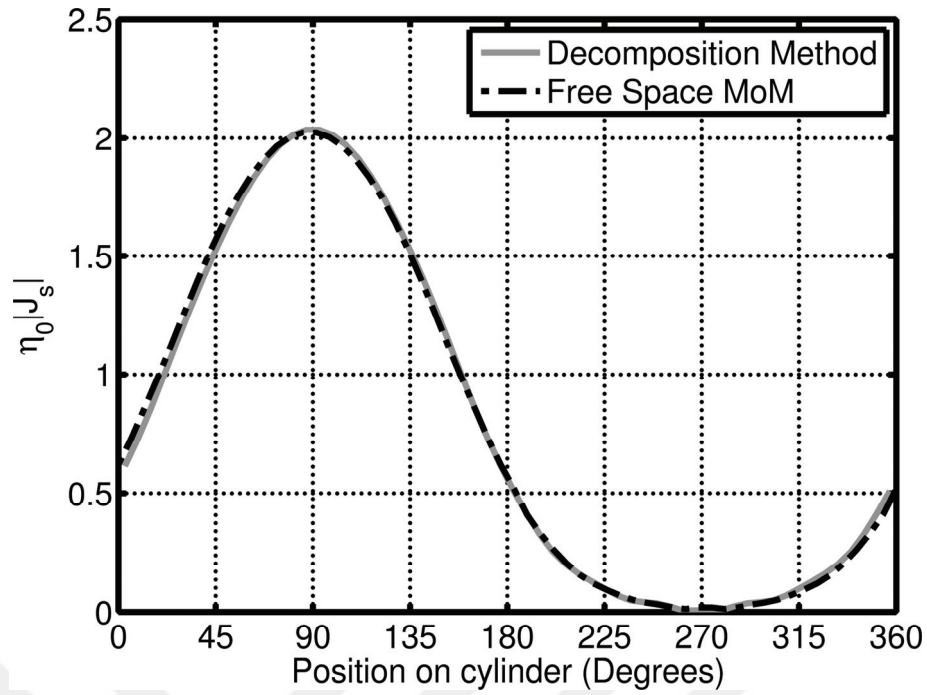


Figure 5.10 Normalized electrical current density induced on a highly electrically conducting circular cylinder half-buried in a material half space with electrical parameters $\epsilon_{r2} = 1$, $\mu_{r2} = 1$ and $\sigma_{e2} = 0$

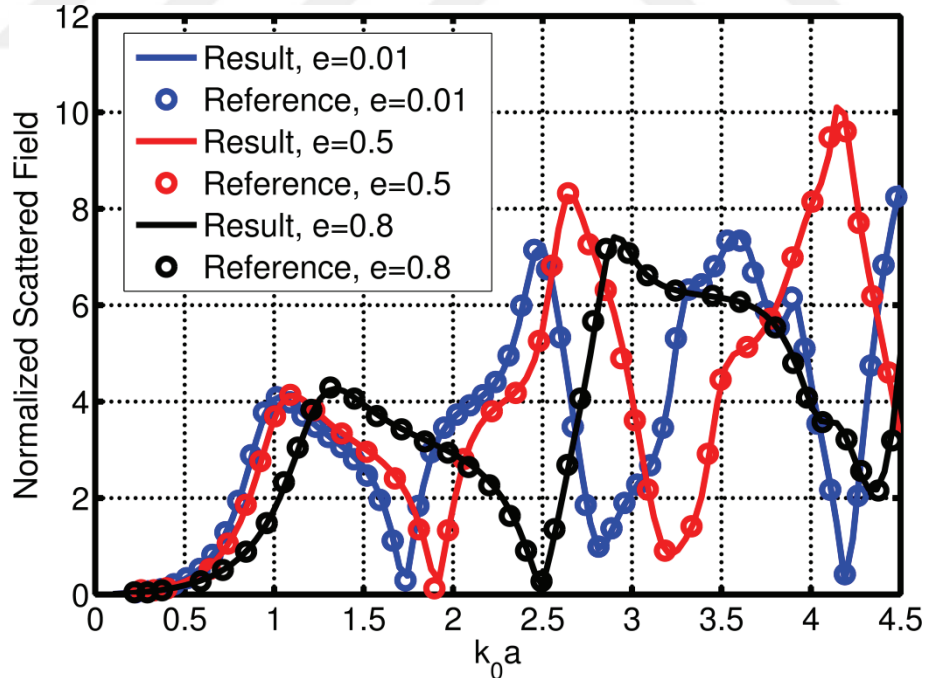


Figure 5.11 Results for monostatic scattering by a semi-buried dielectric elliptical cylinder

Then, bistatic scattering results for a cylinder with elliptical cross section semi-buried in a highly conducting ($\sigma_{e2} = 10^{10}$) half space for $k_0 a = 2\pi$ with different sinusoidal

surface profile amplitude values are presented on Figure 5.12 compared with the reference result on [16]. In this scenario, a plane wave is incident on the scattering object, which has a relative dielectric constant of $\epsilon_{r1} = 4$ and eccentricity value of $e = 0.01$ with an angle of $\phi^i = 60^\circ$. Here, the period of the sinusoidal profile is taken as $L = \lambda$.

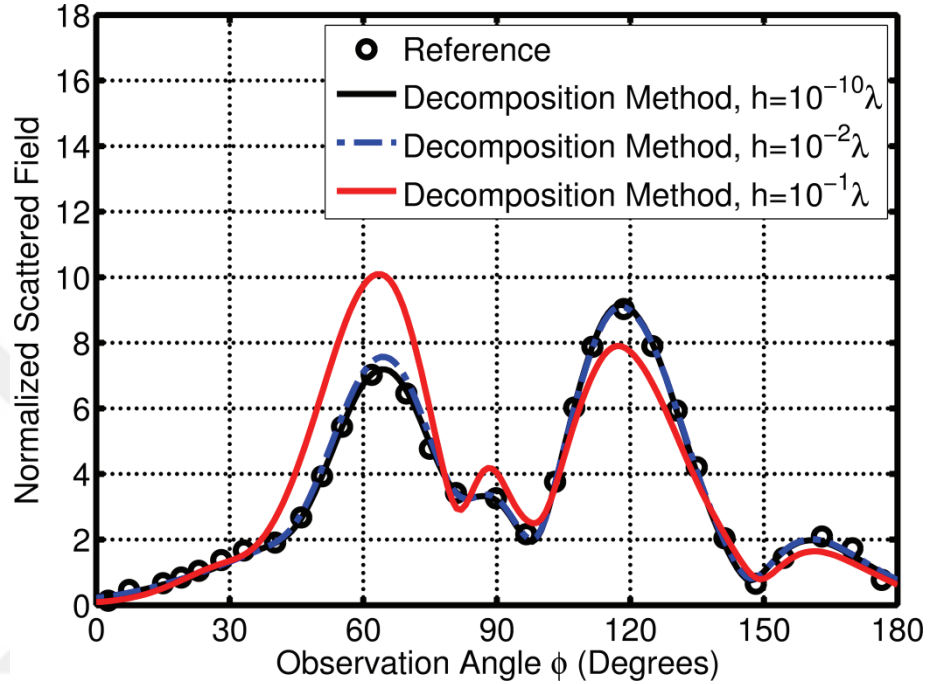


Figure 5.12 Results for bistatic scattering by a semi-buried dielectric elliptical cylinder. As can be seen from the Figure 5.12, reference result and the result calculated for a surface profile with a peak amplitude of $h=10^{-10}\lambda$ are almost indistinguishable, whereas as the h value increases results start to deviate.

Lastly, monostatic scattering width of a circular dielectric cylinder of radius λ with material parameters $\epsilon_{r1} = 2$, $\mu_{r1} = 1$, and $\sigma_{e1} = 0$ semi-buried in a dielectric half space with electrical parameters $\epsilon_{r2} = 4$, $\mu_{r2} = 1$, and $\sigma_{e2} = 0$ shown on Figure 5.13 is investigated. Half space has an interface with a sinusoidal height profile, and calculations are performed for different peak surface profile amplitude values. Results are given on Figure 5.14.

The calculation result of $h=10^{-10}\lambda$ can be considered to correspond to the flat interface case. As can be seen from Figure 5.14, the results of $h=10^{-3}\lambda$ and $h=10^{-10}\lambda$

is almost identical. On the other hand, as the h value increases, difference between the results increases.

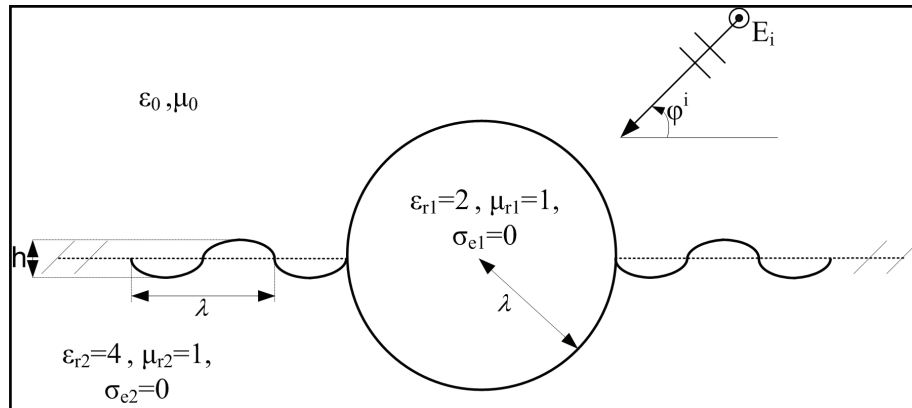


Figure 5.13 Scattering geometry for monostatic scattering by a semi-buried dielectric circular cylinder

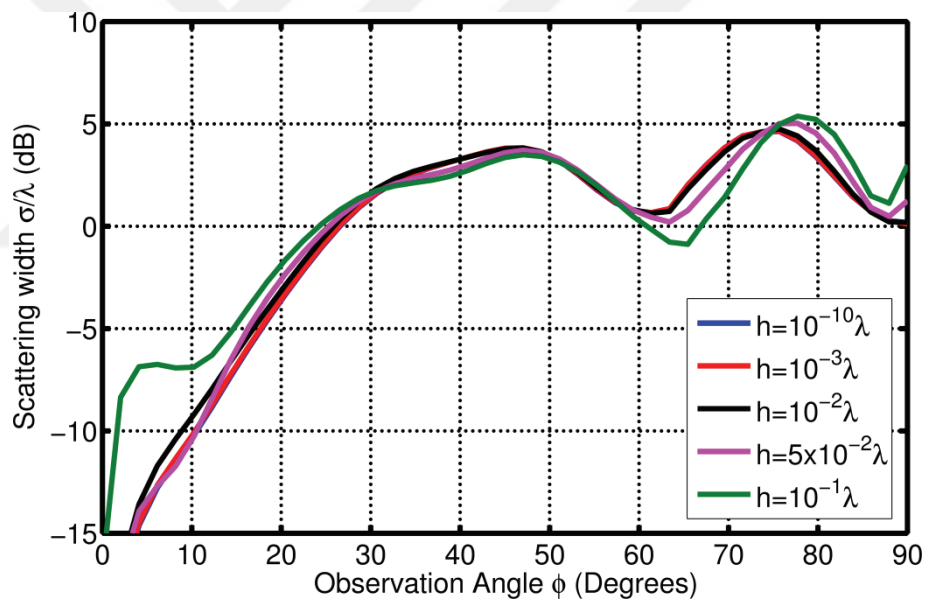


Figure 5.14 Scattering width of a circular cylinder with electrical properties $\epsilon_{r1} = 2$, $\mu_{r1} = 1$ and $\sigma_{e1} = 0$, semi-buried in a half space with electrical properties $\epsilon_{r2} = 4$, $\mu_{r2} = 1$ and $\sigma_{e2} = 0$

CHAPTER 6

CONCLUSIONS

In this thesis, a novel solution method for solving electromagnetic scattering from a perfectly conducting or dielectric object partially buried in a dielectric or perfectly conducting half space is introduced. Formulation for TM_z polarization is explained with example numerical results. The surface equivalence principle and a decomposition method are used to get a set of integral equations for calculating the unknown electric and magnetic current densities on the scatterer and a finite region on the interface of the dielectric half space. Then current densities are calculated from integral equations by the Method of Moments. The scatterer is modeled as a two-dimensional cylindrical object with arbitrary cross section, and the interface between dielectric half space and free space is chosen to be flat or periodic with an arbitrary surface profile.

The Decomposition method is employed to solve scattering from a bump or a cavity on a perfectly conducting infinite ground plane with a flat interface in Chapter 2. Then, in Chapter 3 and Chapter 4, surface equivalency principle and a decomposition method are employed to solve plane wave scattering from an overfilled cavity embedded in a perfectly conducting ground plane and a perfectly conducting cylinder partially buried in a dielectric half space with a flat interface. Lastly, in Chapter 5 the main problem, electromagnetic scattering of a partially buried dielectric cylinder at the dielectric rough surface interface is investigated. It is shown that if appropriate truncation width is chosen, for all the five afore mentioned problems can be solved very accurately with the new solution technique.

In the future, these problems will be solved for TE_z polarization and solution method is thought to be extended to solve three-dimensional problems.

REFERENCES

- [1] Butler, C., (1984). "Current induced on a conducting strip which resides on the planar interface between two semi-infinite half-spaces". IEEE transactions on antennas and propagation, 32(3): 226-231.
- [2] Butler, C., Xu, X.B., and Glisson, A., (1985). "Current induced on a conducting cylinder located near the planar interface between two semi-infinite half-spaces", IEEE transactions on antennas and propagation, 33(6): 616-624.
- [3] Michalski, K.A., and Butler, C.M., (1987). "Evaluation of Sommerfeld integrals arising in the ground stake antenna problem", In IEE Proceedings H-Microwaves, Antennas and Propagation, 134(1): 93-97.
- [4] Marx, E., (1989). "Scattering by an arbitrary cylinder at a plane interface: broadside incidence", IEEE transactions on antennas and propagation, 37(5): 619-628.
- [5] Zu, X.B., and Butler, C.M., (1990). "Current induced by TE excitation on coupled and partially buried cylinders at the interface between two media", IEEE Transactions on Antennas and Propagation, 38(11): 1823-1828.
- [6] Hochman, A., and Leviatan, Y., (2010). "A numerical methodology for efficient evaluation of 2D Sommerfeld integrals in the dielectric half-space problem", IEEE Transactions on Antennas and Propagation, 58(2): 413-431.
- [7] Ling, R. T., and Ufimtsev, P. Y. (2001). "Scattering of electromagnetic waves by a metallic object partially immersed in a semi-infinite dielectric medium", IEEE Transactions on Antennas and Propagation, 49(2): 223-233.
- [8] Michalski, K. A., and Mosig, J. R., (1997). "Multilayered media Green's functions in integral equation formulations", IEEE Transactions on Antennas and Propagation, 45(3): 508-519.
- [9] Wang, X.A., Gan, Y.B., and Li, L. W. (2004). "TE scattering from PEC object partially embedded at dielectric rough surface interface", MSMW'04 Symposium Proceedings, 21-26 June, 2004, Kharkov, Ukraine.
- [10] Wang, X., Gan, Y.B., and Li, L.W., (2003). "Electromagnetic scattering by partially buried PEC cylinder at the dielectric rough surface interface: TM case", IEEE Antennas and Wireless Propagation Letters, 2(1): 319-322.
- [11] Kizilay, A., and Rothwell, E., (1999). "Efficient computation of transient TM scattering from a cylinder above an infinite periodic surface", Journal of electromagnetic waves and applications, 13(7): 943-961.

- [12] Kizilay, A., (2000). A perturbation method for transient multipath analysis of electromagnetic scattering from targets above periodic surfaces, Doctoral dissertation, Michigan State University, E. Lansing, MI.
- [13] Makal S., (2011). Computation of the scattered fields from a dielectric object buried in a medium with a periodic surface by a decomposition method, Doctoral dissertation, Yıldız Technical University, İstanbul.
- [14] Harrington, R.F., (2001) Time-Harmonic Electromagnetic Fields., IEEE press., New York.
- [15] Hinders, M.K., and Yaghjian, A.D., (1991). “Dual-series solution to scattering from a semicircular channel in a ground plane”, IEEE microwave and guided wave letters, 1: 239-242.
- [16] Byun, W.J., Yu, J.W., and Myung, N.H. (1998). “TM scattering from hollow and dielectric-filled semielliptic channels with arbitrary eccentricity in a perfectly conducting plane”, IEEE transactions on microwave theory and techniques, 46(9): 1336-1339.
- [17] Jin, J., (1998). “Electromagnetic scattering from large, deep, and arbitrarily-shaped open cavities”, Electromagnetics, 18(1): 3-34.
- [18] Chumachenko, V.P., Karacuha, E., and Dumanlı, M., (2000). “TM-scattering from a multiangular groove in a ground plane”, Journal of electromagnetic waves and applications, 14(3): 329-347.
- [19] Tyzhnenko, A., (2004). “Two-dimensional TE-plane wave scattering by a dielectric-loaded semicircular trough in a ground plane”, Electromagnetics, 24(5): 357-368.
- [20] Tyzhnenko, A.G., and Ryznik, Y.V. “A unique solution for H-scattering from 2-D roughness on a pec plane”, 18th International Conference on Applied Electromagnetics and Communications, 12-14 October 2005, Dubrovnik, Croatia.
- [21] Kolbehdari, M.A., Auda, H.A., and Elsherbeni, A.Z., (1989). “Scattering from a dielectric cylinder partially embedded in a perfectly conducting ground plane”, Journal of Electromagnetic Waves and Applications, 3(6): 531-554.
- [22] Pérez-Arancibia, C., and Bruno, O.P., (2014). “High-order integral equation methods for problems of scattering by bumps and cavities on half-planes”, JOSA A, 31(8): 1738-1746.
- [23] Wood, A., (2006). “Analysis of electromagnetic scattering from an overfilled cavity in the ground plane”, Journal of Computational Physics, 215(2): 630-641.
- [24] Saynak, U., and Kizilay, A., (2016). “Computation of the scattered fields from an arbitrary discontinuity on a perfectly conducting ground plane by a decomposition method”, Turkish Journal of Electrical Engineering & Computer Sciences, 24(3).
- [25] Norman, A., Nyquist, D., Rothwell, E., Chen, K.M., Ross, J., and Ilavarasan, P., (1996). “Transient scattering of a short pulse from a conducting sinusoidal surface”, Journal of electromagnetic waves and applications, 10(4): 461-487.

- [26] Zaki, K., and Neureuther, A., (1971). "Scattering from a perfectly conducting surface with a sinusoidal height profile: TE polarization", IEEE Transactions on Antennas and Propagation, 19(2): 208-214.



CALCULATION OF SELF TERMS

In the calculation of equations (2.28) and (3.7) for $\bar{\rho}_n \rightarrow \bar{\rho}_m$ calculation is cannot be performed by numerical integration because of singularity and discontinuity of the integrand. Calculation can be performed by adding and subtracting singular part [14] of the Hankel function:

$$\int_{-\Delta/2}^{\Delta/2} H_0^{(2)}(k|l'|) dl' = 2 \int_0^{\Delta/2} \left\{ H_0^{(2)}(k|l') - \left[1 - j \frac{2}{\pi} \ln \left(\frac{\gamma k l'}{2} \right) \right] \right\} dl' + 2 \int_0^{\Delta/2} \left[1 - j \frac{2}{\pi} \ln \left(\frac{\gamma k l'}{2} \right) \right] dl'. \quad (\text{A.1})$$

Here γ is the Euler constant. First term on right hand side of (A.1) is can be calculated numerically because of smooth behavior of the integrand, and second term is calculated analytically as

$$2 \int_0^{\Delta/2} \left[1 - j \frac{2}{\pi} \ln \left(\frac{\gamma k l'}{2} \right) \right] dl' = -\frac{2\Delta}{\pi} \left[\frac{\pi}{2} + j - j \ln \left(\frac{\gamma k \Delta}{4} \right) \right]. \quad (\text{A.2})$$

So

$$Z(k, \eta, S_n, S_n) \cong \frac{k\eta}{2} \int_0^{\Delta_n/2} \left\{ H_0^{(2)}(k|l') - \left[1 - j \frac{2}{\pi} \ln \left(\frac{\gamma k l'}{2} \right) \right] \right\} dl' - \frac{2\Delta_n}{\pi} \left[\frac{\pi}{2} + j - j \ln \left(\frac{\gamma k \Delta_n}{4} \right) \right]. \quad (\text{A.3})$$

In the calculation of the equation (3.7), during the integration while $\bar{\rho}_n \rightarrow \bar{\rho}_m$, $H_1^{(2)}\left(k \left\| \bar{\rho}_m - (\bar{\rho}_n + l' \hat{I}_n) \right\| \right)$ will vary rapidly when $\bar{\rho}_n$ gets close to $\bar{\rho}_m$. The integration should be carefully evaluated since $k \left\| \bar{\rho}_m - (\bar{\rho}_n + l' \hat{I}_n) \right\| \rightarrow 0$.

$$\begin{aligned}
& \lim_{\vec{\rho}_m \rightarrow \vec{\rho}_n} \int_{l'=-\Delta_n/2}^{\Delta_n/2} H_1^{(2)} \left(k \left\| \vec{\rho}_m - (\vec{\rho}_n + l' \hat{I}_n) \right\| \right) \frac{\hat{n}_n \cdot (\vec{\rho}_n - \vec{\rho}_m)}{\left\| \vec{\rho}_m - (\vec{\rho}_n + l' \hat{I}_n) \right\|} dl' \\
&= \lim_{\vec{\rho}_m \rightarrow \vec{\rho}_n} \int_{l'=-\Delta_n/2}^{\Delta_n/2} H_1^{(2)} \left(k \left\| \vec{\rho}_m - (\vec{\rho}_n + l' \hat{I}_n) \right\| \right) \cos \psi dl'
\end{aligned} \tag{A.4}$$

From Figure A.1

$$\cos \psi = \frac{\delta}{\sqrt{\delta^2 + s'^2}} \tag{A.5}$$

For small arguments Hankel function can be approximated as [14]

$$H_1^{(2)} \left(k \left\| \vec{\rho}_m - (\vec{\rho}_n + l' \hat{I}_n) \right\| \right) = H_1^{(2)} \left(k \sqrt{\delta^2 + s'^2} \right) \cong \frac{2j}{\pi k \sqrt{\delta^2 + s'^2}}. \tag{A.6}$$

Substituting (A.6) and (A.5) into (A.4) yields

$$\begin{aligned}
& \lim_{\vec{\rho}_m \rightarrow \vec{\rho}_n} \int_{l'=-\Delta_n/2}^{\Delta_n/2} H_1^{(2)} \left(k \left\| \vec{\rho}_m - (\vec{\rho}_n + l' \hat{I}_n) \right\| \right) \cos \psi dl' \\
&\cong \frac{2j}{\pi k} \lim_{\delta \rightarrow 0} \int_{l'=-\Delta_n/2}^{\Delta_n/2} \frac{1}{\sqrt{\delta^2 + s'^2}} \frac{\delta}{\sqrt{\delta^2 + s'^2}} dl' = \frac{2j}{k}
\end{aligned} \tag{A.7}$$

So equation (3.7) is can be calculated for $\vec{\rho}_n \rightarrow \vec{\rho}_m$ as

$$K(k, S_n, S_n) = -\frac{1}{2}. \tag{A.8}$$

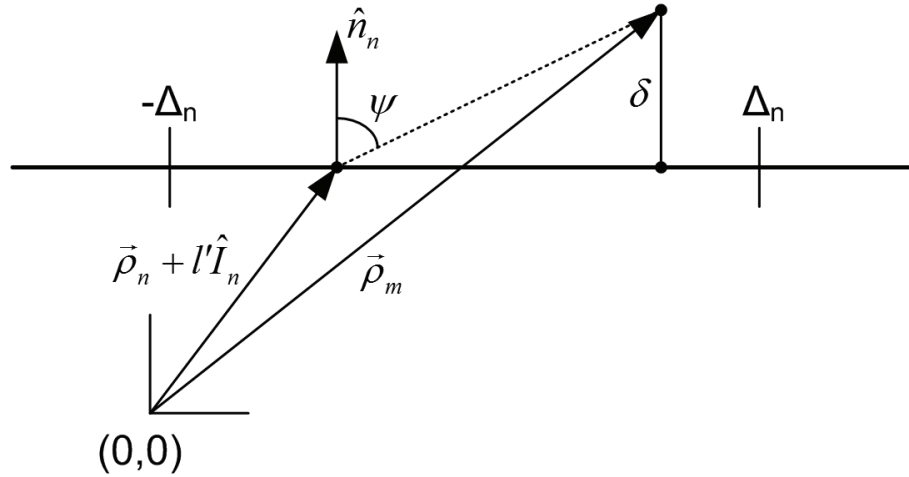


Figure A.1 Evaluation of Principle Value

CURRICULUM VITAE

PERSONAL INFORMATION

Name Surname : Uğur SAYNAK
Date of birth and place :29/03/1981-Nazilli
Foreign Languages :English
E-mail :ugur.saynak@tubitak.gov.tr

EDUCATION

Degree	Department	University	Date of Graduation
Ph.D.	Electronics and Communications Engineering	Yıldız Technical University	2016
M.S	Electronics and Communications Engineering	İzmir Institute of Technology	2008
B.S	Electronics and Communications Engineering	Süleyman Demirel University	2003
High School	Science and Math	Private Fatih Sultan High School	1998

WORK EXPERIENCE

Year	Corporation/Institute	Enrollment
2007-	TUBİTAK	Senior Researcher
2005-2007	İzmir Institute of Technology	Researcher



PUBLISHERMENTS

Papers

1. Saynak, U., and Kizilay, A., (2016). "Computation of the scattered fields from an overfilled cavity embedded in a perfectly conducting ground plane", *Journal of Electromagnetic Waves and Applications*, 1-10.
2. Saynak, U., and Kizilay, A., (2016). "Computation of the scattered fields from an arbitrary discontinuity on a perfectly conducting ground plane by a decomposition method", *Turkish Journal of Electrical Engineering & Computer Sciences*, 24(3).
3. Saynak, U., Karahan, H. A., Coskun, A. F., Yucedag, S. M., Aldirmaz, S., Karabayir, O., ... and Bati, O., (2014). "Preliminary set of analysis for the assessment of wind turbines which are in the line-of-sight of radar, navigation and communications systems", *IET Radar, Sonar & Navigation*, 8(5): 415-424.
4. Saynak, U., and Kustepeli, A., (2009). "Novel square spiral antennas for broadband applications", *Frequenz*, 63(1-2): 14-19.

Conference Papers

1. Kizilay, A., and Saynak, U., (2016). "Scattering From a Conducting Cylinder Partially Buried in A Dielectric Half Space by a Decomposition Method", in *Proc. of MIKON 2016*, 10-12 May 2016, Krakow, Poland.
2. Karabayir, O., Saynak, U., Coşkun, A. F., Bıyık, M., Batı, B., Batı, Ö., Serim, H.A., Kent S., (2016). "Synthetic Aperture Radar (SAR) Imaging of Complex Scenes Considering Near Field Scattering Characteristics", in *Proc. of EUSAR 2016*, 06-09 June 2016, Hamburg, Germany.
3. Coşkun, A.F., Saynak, U., Karabayir, O., Bıyık, M., Batı, B., Batı, Ö., and Serim, H. A., (2015). "Statistical modeling of wind turbines' bi-static free-space scattering characteristics for UHF-band applications", In *Microwave Symposium (MMS)*, 2015, 30 November-2 December 2015, Lecce, Italy.
4. Karabayir, O., Unal, M., Coskun, A. F., Yucedag, S. M., Saynak, U., Bati, B., ... and Kent, S., (2015). "CLEAN based wind turbine clutter mitigation approach for pulse-Doppler radars", In *2015 IEEE Radar Conference (RadarCon)*, 10-15 May 2015, Arlington, VA, USA.
5. Aldirmaz, S., Saynak, U., Karabayir, O., Coşkun, A. F., Serim, H., Karahan, Ş., ... and Bölükbaş, D., (2013). "Wind turbine effects on radar performance", In *Signal Processing and Communications Applications Conference (SIU) 2013*, 24-26 April 2013, Lefkosa, North Cyprus.
6. Saynak, U., Bölükbaş, D., Çolak, A., Tayyar, İ.H. and Özdemir, C., (2010) "Rüzgar Türbinlerinin Zamana Bağlı Radar Kesit Alanı Değişimi ve Zaman-Frekans Analizi", *URSI-TÜRKİYE '2010 Bilimsel Kongresi*, 25-27 August 2010, Güzelyurt, Kıbrıs.

7. Saynak, U., Çolak, A., Bölükbaş, D., Tayyar, İ. H., and Özdemir, C., (2010). “Utilizing ISAR imagery to analyze the diffraction effects from leading and trailing edges of a target”, In 2010 10th Mediterranean Microwave Symposium, 25-27 August 2010, Güzelyurt, Kıbrıs.
8. Bölükbaş, D., Saynak, U., Çolak, A., Tayyar, I.H., and Özdemir, C., (2009) “Rüzgar Tribünlerinin Radarlara Etkisinin Analizi”, RÜGES 2009, 4-5 June 2009, Samsun, Turkey.
9. Saynak, U., Colak, A., Avcıbaşı, Y., Bölükbaş, D., Tayyar, I.H., and Ozdemir, C., (2008). “İletken ve Dielektrik Yüklü Karmaşık Hedeflerin Radar Kesit Alanlarının Hesaplanması ve 2-Boyutlu Ters Yapay Açıklıklı Radar İmgelerinin Çıkartılması”, URSI-TÜRKİYE '2008 Bilimsel Kongresi, 20-22 October 2008, Antalya, Turkey.
10. Saynak, U., Colak, A., Avcıbaşı, Y., Bölükbaş, D., Tayyar, I.H., and Ozdemir, C., (2008). “2-D ISAR imaging of complex objects using shooting-bouncing ray (SBR) and physical theory of diffraction (PTD) techniques”, In V. Intern. Workshop on Electromagn. Wave Scattering, 20-22 October 2008, Antalya, Turkey.
11. Saynak, U., Çolak, A., Avcıbaşı, Y., Bölükbaş, D., Tayyar, İ.H., and Özdemir, C., (2008)., “Seiken ışın yöntemiyle büyük ve karmaşık platformlardan saçılma hesabı ve nümerik uygulamaları”, Savtek 2008, 26-27 June 2008, METU, Ankara.
12. Saynak, U., and Kuştepelı, A., (2007). “A Novel Square-Spiral Strip Antenna”, ITG-Fachbericht-INICA 2007, 28-30 March 2007, Munich, Germany.
13. Saynak, U., & Kuştepelı, A. (2006). “Dikdörtgen Spiral Antenler Üzerine Bir İnceleme”, ELECO 2006, 6-10 December 2006, Bursa, Turkey.
14. Saynak, U., and Kuştepelı, A., (2006). “Dikdörtgen Spiral Anten Tasarımında Yeni Bir Yaklaşım” URSI-TÜRKİYE '2006 Bilimsel Kongresi, 1-3 September 2006, Ankara, Turkey.